Spring 2021

Asymmetry in Mie scattering by a homogeneous sphere

Samuel Hanna
shanna@rollins.edu

Recommended Citation

Hanna, Samuel, "Asymmetry in Mie scattering by a homogeneous sphere" (2021). *Honors Program Theses*. 140.
https://scholarship.rollins.edu/honors/140

ROLLINS COLLEGE

HONORS THESIS

Asymmetry in Mie scattering by a homogeneous sphere

Author:
Samuel HANNA

Supervisor:
Dr. Ashley CANNADAY

A thesis submitted in fulfillment of the requirements
for the degree of Artium Baccalaureus Honoris

in the

Department of Physics

April 13, 2021

Acknowledgements

A special thank you to:

Dr. Ashley Cannaday of the Rollins College Department of Physics for supervising the completion of this thesis,

Dr. Thomas Moore and Dr. Pamela Brannock of the Rollins College departments of Physics and Biology, respectively, for committing their time to reviewing this thesis and the process of its completion,

Rollins College for facilitating this research.

Contents

List of Figures

Chapter 1

Introduction

The scattering of light by small particles is a common phenomenon. It is on display throughout the daily lives of most individuals. For example, Rayleigh scattering of sunlight by particles in Earth's atmosphere is the mechanism behind the sky's blue color[1]. Waves of light incident on a particle can be scattered elastically or inelastically. In the former case, these waves do not transfer any energy to the scatterer, while in the latter case they do. Raman scattering, which is an example of inelastic scattering, is commonly used by chemists to determine the composition of a substance. Certain wavelengths of light are scattered inelastically by different elements and compounds in higher proportions than other wavelengths. Light scattered inelastically by a substance can be collected and resolved into its constituent wavelengths, and the proportions in which each wavelength is present can be determined. The particular wavelengths which a substance scatters in high proportions are unique to that substance, so the inelastic scattering from an unknown substance can be compared to scattering by known substances, and the unknown substance can be identified based on the closest match[2]. Rayleigh scattering, such as that mentioned previously, is elastic scattering which occurs when the dimensions of the scatterer are far less than the wavelength of the incident light. Elastic scattering by particles with dimensions on the order of the wavelength of the incident light is called Mie scattering[3]. During Mie scattering, which is the focus of this thesis, the incident light scatters off of a scatterer at all angles, but is directed largely in the forward direction, that is at angles less than 90° with respect to the optical axis, which is the axis along which light (in this case, the beam incident on the scatterer) travels through a system. A cross section of the Mie scattered intensity pattern in a plane orthogonal to the optical axis exhibits a characteristic pattern of ripples representing regions of high and low intensity, which can be seen in figure 1.1. The spacing of these ripples is dependent on the refractive indices of both the scatterer and its surrounding medium, the wavelength of the incident light, and the size of the scatterer. Figure 1.1 is an image, called a scattergram, depicting the intensity of light scattered elastically by a polystyrene bead at angles up to 55° with respect to the optical axis. The bead had a diameter of approximately 5μm and the light had a wavelength of 532nm. The center of a scattergram represents an angle of 0° with respect to the optical axis, while points on the scattergram which are increasingly farther from the center represent increasing scattering angles, θ. The azimuthal angle, ϕ, varies with rotation about the optical axis, which is normal to the center of the scattergram. This coordinate system is shown in relation to a scattergram in figure 1.2. The center of experimental scattergrams is typically dark because in most cases the majority of light incident on a scatterer passes through without deviating, and a mask or other device is often used to obstruct this unscattered light from reaching the detector and causing overexposure, artifacts, or other undesirable effects.

Mie scattering can be used to obtain morphological information about a specimen. Most commonly, light with a known wavelength is scattered by a specimen with a known refractive index which is surrounded by a medium with a known refractive index, and the irradiance of light at each scattering angle is recorded. Experimental scattering data can be compared to simulated scattering for scatterers with a range of diameters, and the size corresponding to the simulated scattering which is most similar to the experimental data used as an estimate for the size of the specimen.

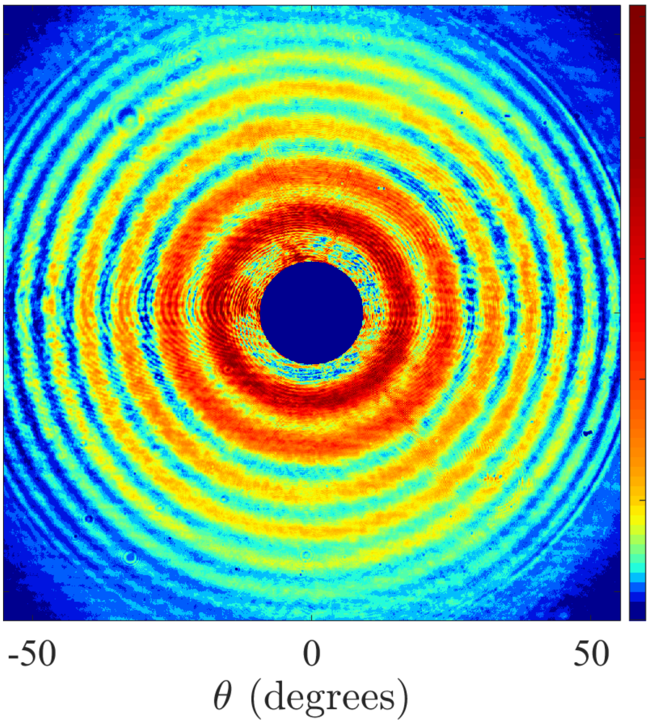

FIGURE 1.1: A scattergram depicting the irradiance of light with a wavelength of 532nm scattered at angles out to 55° by a 5µm polystyrene bead surrounded by air. Deep blue indicates the lowest irradiance and crimson indicates the highest.

Both theoretical and empirical scattergrams have been published in the existing literature surrounding angular scattering theory and its applications, a review of which is provided in Chapter 2. All of the scattergrams of forward scattered light exhibit the characteristic pattern of amplitude maxima and minima which appear as concentric ripples, but vary due to differences in the wavelength and polarization of the incident light, the refractive indices of the scatterer and its surrounding medium, and the diameter of the scatterer. For instance, an increase in scatterer size or the refractive index of the medium surrounding the scatterer leads to a decrease in the angular

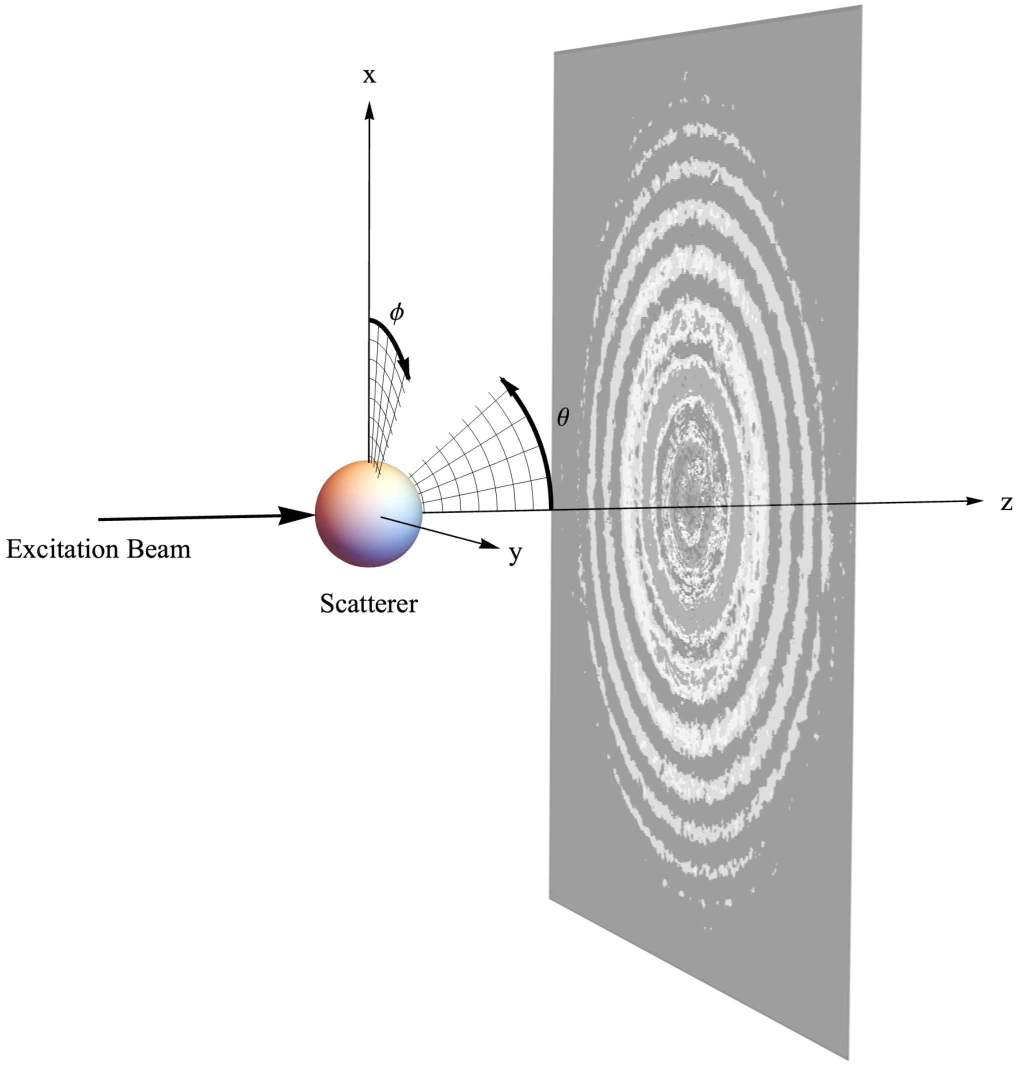

FIGURE 1.2: Spherical and cartesian coordinate systems in relation to a scattergram. A spherical scatterer is shown at the origin, and the excitation beam propagates along the z-axis, which is identical to the optical axis and is normal to the center of the scattergram. The center of the scattergram represents a scattering polar angle θ of 0^o, and points which are increasingly farther from the center of the scattergram represent increasing θ. The azimuthal angle, ϕ, is measured from the x-axis and varies with rotation about the z-axis.

spacing between ripples and therefore the presence of more ripples within the same angle range. Mie scattering patterns from a given wavelength of incident light are more sensitive to changes in scatterer size than to changes in refractive index. Chapter 2 will discuss how Mie scattering patterns can

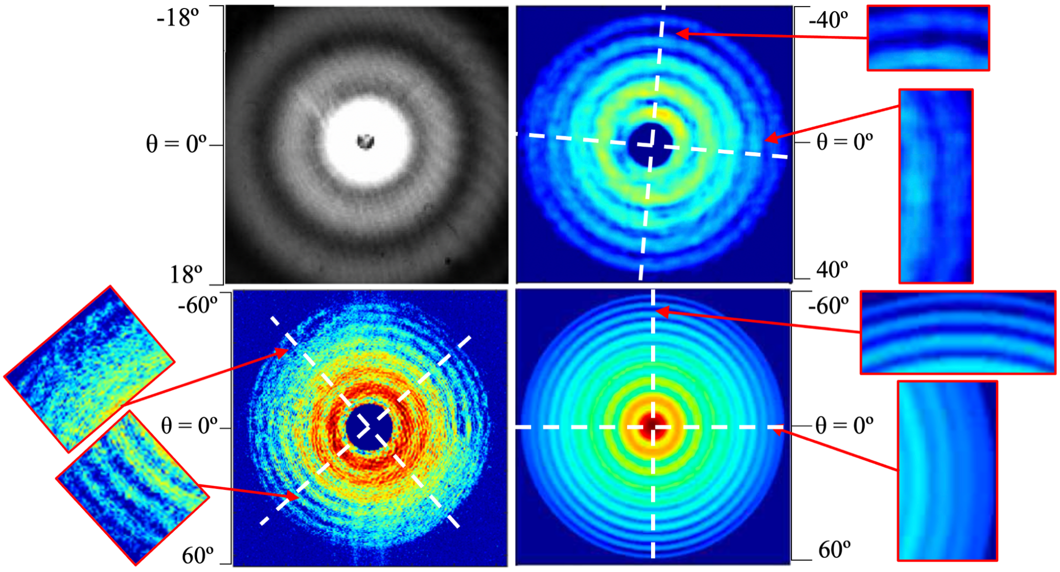

FIGURE 1.3: Top left: Scattering by a 4µm polystyrene bead, published by Cottrell, et al.[4]. Top right: Scattering by a polystyrene bead with estimated diameter of 4.4µm, published by Smith and Berger[5]. Bottom left: Scattering by a polystyrene bead with estimated diameter of 5µm, published by Cannaday, et al.[6]. Bottom right: Simulated scattering by a 6µm polystyrene sphere, published by Smith in his doctoral thesis[7]. All scattergrams depict the irradiance of light scattered at various angles with respect to the optical axis. Approximate axes of mirror-symmetry are shown on three of the scattergrams with dotted lines. Insets show portions of the scattergrams in which the asymmetry is particularly visible.

be analyzed in order to obtain information about the scatterer.

A collection of scattergrams published in existing literature, from spherical scatterers ranging in diameter from approximately 4µm to 6µm, is presented in figure 1.3. Some of the scattergrams, both theoretically produced and empirically obtained, exhibit azimuthal asymmetry, even though they depict scattering by a spherical (and therefore symmetrical) specimen. In two quadrants of the scattergrams, the scattered irradiance falls to a lower value between ripples than in the other two. This gives the ripples an elliptical appearance, but they are not elongated to a measurable degree. The two axes over which the scattergram is symmetrical are orthogonal and lie on the plane of the scattergram, as shown by dashed lines in figure 1.3.

The scattergram at the top left of figure 1.3 was published by Cottrell et al. and depicts the irradiance across a range of angles of light with a wavelength of 457.9nm scattered by a fluorescent, polystyrene microsphere with a nominal diameter of 4µm surrounded by distilled water[4]. Over the relatively small angle range included in this scattergram, from approximately 0^{o} to 18^{o}, there is no clear asymmetry exhibited which is not attributable to noise or artifacts from the mask. However, this is likely due to the relatively small angle range depicted because, as can be seen in the other scattergrams, the asymmetry is more pronounced at higher angles. The scattergram at the top right was published by Smith and Berger and depicts the irradiance over a range of angles from approximately 0^{o} to 45^{o} of light with a wavelength of 785nm scattered by a polystyrene bead with an estimated diameter of 4.372µm surrounded by deionized water[5]. Asymmetry is clearly visible in this scattergram, particularly in the areas highlighted in the figure. The scattergram in the bottom left was published by Cannaday et al. and depicts scattering over a range of angles from approximately 0^{o} to 60^{o} of light with wavelength 785nm by a polystyrene bead with an estimated diameter of 4.94µm suspended in water[6]. Asymmetry is clearly visible in this scattergram as well. Finally, the scattergram in the bottom right was published by Zachary Smith in his doctoral thesis for the University of Rochester and depicts simulated scattering of x-polarized (horizontally polarized) light over a range of angles from approximately 0^o to 60^o by a polystyrene bead with a diameter of 6µm[7]. Asymmetry is also visible in this scattergram.

If this asymmetry were only present in experimental scattergrams or in the scattergrams from a single group of researchers, it could be readily attributed to experimental conditions. However, Mie theory, which mathematically models the electric and magnetic fields of Mie scattered light based on the incident field, predicts that even an idealized plane wave[1] of light will be scattered asymmetrically by a homogeneous sphere centered at the origin. This indicates that the asymmetry is a feature inherent to Mie scattering, which is unexpected given the symmetry of the described scenario. Everything in the Mie theory model is assumed to be perfectly symmetrical about the opical axis except for the incident electromagnetic wave itself, which is polarized in one direction which is orthogonal to the optical axis. This thesis will explain how the asymmetry in Mie scattering patterns is related in theory to the polarization of the incident light and demonstrate this relationship empirically.

1.1 Outline of thesis

The outline of this thesis is as follows:

Chapter 2 provides a brief overview of angular scattering theory and existing research in the field of angular scattering. Measurements of the light scattered by particles can be used to estimate the size of the scatterers, and

---

[1] The plane wave model of light assumes uniform maximum amplitude and irradiance across the light's entire extent, and wavefronts are assumed to be planes to which the direction of propagation is normal.

this technique has been implemented to estimate the size of organelles within single cells.

Chapter 3 presents the mathematical models of Mie scattering developed by Gustav Mie and others and explains why they predict that light scattered by a perfectly spherical particle will be asymmetrical. This arises as a result of the polarization of the incident light, and theory predicts that a rotation in the polarization will lead to a corresponding rotation in the features of the scattering pattern.

Chapter 4 presents experimentally obtained scattergrams depicting scattering by polystyrene beads, which were recorded using an angular scattering microscope. The polarization of the incident light was rotated using a half-wave plate and a linear polarizer, and the irradiance of scattered light over a range of angles was recorded. Experimental scattergrams depicting scattering of light with three different polarization states were then fit to a theoretical model, and the effects of changing polarization on the fits was tested.

To end, Chapter 5 provides the conclusion, discusses the significance of this research, and provides suggestions for further experiments.

Chapter 2

Angular scattering overview and its applications

2.1 Mie theory

When light is incident on a spherical particle with a diameter on the order of the wavelength of light and a different index of refraction than its surrounding medium, the light scatters off of the particle at all angles, as mentioned in Chapter 1. The electric and magnetic fields of the scattered light can be modeled by solutions to Maxwell's equations, which are a set of differential equations that concisely encompass most of modern electromagnetic theory. Gustav Mie, in 1908, published extensive and rigorous work in *Annalen der Physik* which provided exact solutions to Maxwell's equations, in the form of infinite sums, for the case of a linearly-polarized plane wave incident on a perfectly spherical scatterer[8]. These solutions, for the particular case mentioned, form the basis of Mie theory.

Mie scattering patterns vary as a result of factors including the refractive indices of the scatterer and the surrounding medium, the wavelength and polarization of incident light, and the diameter of the scatterer. Mie scattering is particularly sensitive to size changes in the scatterer. Larger scatterers, as compared to smaller scatterers, produce scattering patterns with less angular

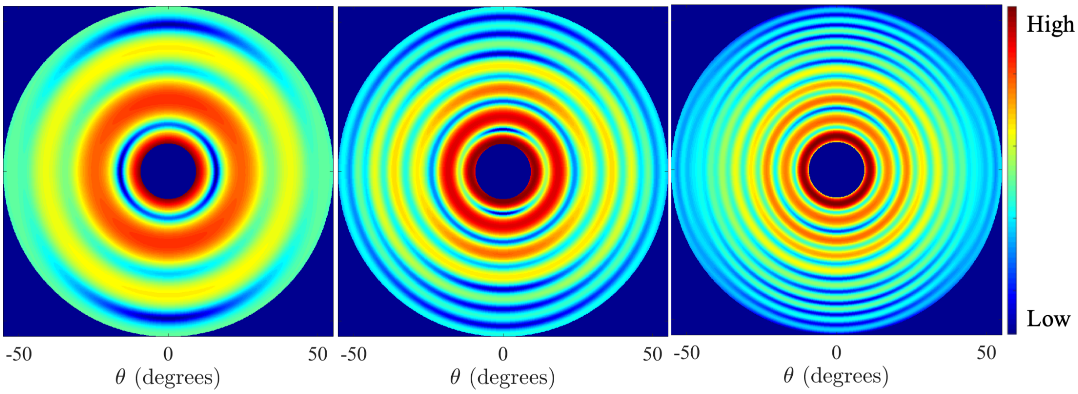

FIGURE 2.1: Simulated scattergrams generated using a Mie theory model for beads with diameters of, left to right, 2µm, 5µm, and 8µm. The wavelength and polarization of the incident light and the refractive indices of the scatterer and its surrounding medium are identical for all three scattergrams. Note that fewer local irradiance maxima are visible within the same angle range in scattergrams from spheres with with increasingly smaller diameters. The colormap used is shown to the right of the scattergrams, where dark blue indicates the lowest scattered irradiance and crimson indicates the highest.

separation between local irradiance maxima. This effect is shown in figure 2.1, which depicts simulated scattergrams generated based on a generalization of Mie theory which accounts for a focused Gaussian excitation beam (this generalized Mie theory is explained in Section 2.3.1). The simulated scatterers were homogeneous spheres with three different diameters, 2µm, 5µm, and 8µm. The simulated excitation beam was linearly polarized in the horizontal direction, and it had a wavelength of 532nm and a beamwaist at the scatterer of 10µm. The scatterers had a refractive index of 1.57826 and were surrounded by a medium with a refractive index of 1.00029. The angular spacing between local irradiance maxima decreases as the size of the scatterer increases.

2.2 Polarization

Electromagnetic waves, including light, consist of oscillating electric and magnetic fields. The two are orthogonal to each other, and both are orthogonal to the direction of the wave's propagation, as shown in figure 2.2. The polarization of a light wave is defined by the orientation of its electric field. Light emitted by a source is comprised of many constituent waves. In most sources, such as the sun or a lightbulb, the constituent waves are each polarized in a random direction. There is therefore no dominant direction in which the electric field oscillates, and the emitted light is called unpolarized light. In the case of a linearly polarized beam, the electric fields of all constituent waves oscillate in the same direction. A device called a linear polarizer (LP) can be used to produce linearly polarized light from any source by blocking all portions of a beam except those with an electric field oscillating in one particular direction, along what is called its transmission axis (TA). Mie theory assumes a linearly polarized plane wave as the excitation beam which is incident on a spherical scatterer at the origin[8]. This scenario is depicted in figure 2.2.

A wave of any possible polarization can be represented as the superposition of two orthogonal polarization states[9]. Furthermore, Bohren and Huffman explain that, because of the linearity of Maxwell's equations, when two incident polarization states are superposed to represent an arbitrary polarization state, the solutions to Maxwell's equations for the two constituent polarization states can be superposed to produce a solution for the arbitrary polarization state. Therefore, solutions to Maxwell's equations for any arbitrary polarization state can be readily extrapolated after a given scattering problem has been solved twice for two orthogonal polarization states[9]. The electric fields represented by the solutions for the two orthogonal polarization states are superposed in the proper proportion, based on the proportions

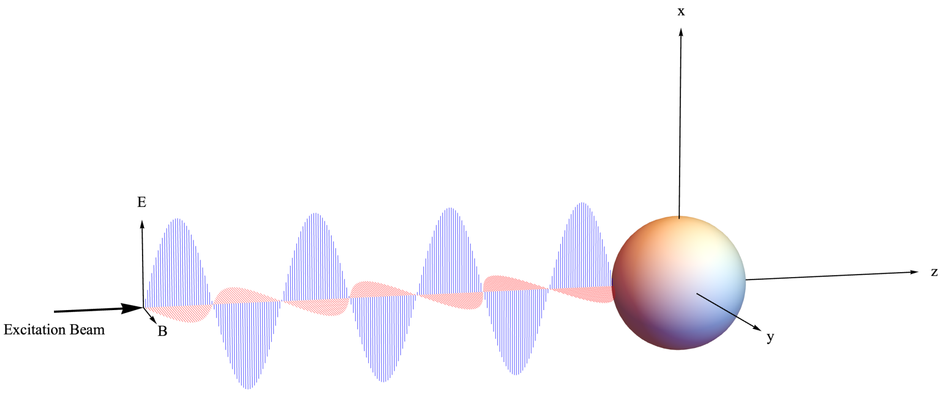

FIGURE 2.2: In Mie theory, a plane wave excitation beam is incident on a small sphere centered at the origin[8]. Shown here is an x-polarized excitation beam propagating along the z-axis. Its electric field, E, points along the x-axis, and its magnetic field, B, correspondingly points along the y-axis.

of orthogonally polarized electric fields which must be superposed to represent the arbitrarily polarized electric field of the problem.

2.3 Size Estimation

Consider light of a given wavelength and polarization incident on a homogeneous, spherical scatterer with a given refractive index surrounded by a uniform medium with a different refractive index. The Mie scattering pattern produced under these particular conditions is distinctive to the size of the scatterer. Furthermore, small size changes (on the order of nanometers) in the scatterer result in significant changes to the Mie scattering pattern. These principles have been applied to obtain size information about cell organelles, as explained in Section 2.3.2.

An estimate for the diameter of the scatterer considered above can be extracted from a recorded angular scattering pattern if the wavelength and polarization of the excitation beam and the refractive indices of the scatterer and its surrounding medium are known. Based on solutions to Maxwell's equations, such as those of Mie theory, simulated scattering patterns can be generated for spherical particles spanning a size range known to encompass the size of the specimen, in regular increments. The simulated scattering patterns for each size of scatterer can be compared to the empirical data, and the diameter of the specimen can be estimated based on the closest match.

Because Mie scattering patterns are sensitive to changes in scatterer size, angular scattering is particularly useful for detecting size changes in a specimen over time. Size changes on the order of nanometers can be observed, which is smaller than the resolution of typical optical microscopy. Furthermore, angular scattering techniques do not require that any alterations be made to the specimen, such as the addition of fluorescent tags or other chemicals.

2.3.1 Generalized Lorenz-Mie theory

It is common to use laser light as the illumination beam when collecting scattering data, since it can be relatively monochromatic, polarized, and high-intensity. The Gaussian beam of a single mode laser can be well approximated as a plane wave when the beam has a large diameter and is well-collimated, which means that the beam diameter is approximately constant at different points along the beam. However, it is sometimes beneficial when using angular scattering to obtain size estimates to condense the laser beam down to a spot with a diameter close to that of the scatterer. In this case, the beam is not collimated and the laser is not well approximated as a plane wave, and therefore Mie theory (which, as mentioned previously, assumes plane wave illumination) is an inadequate model for the scattering. However, the incident beam can be represented as the superposition of monocromatic plane waves, and (because of the linearity of Maxwell's equations) the scattered electric and magnetica fields from such a beam can be modeled as the superposition of the scattered fields from those plane waves[10]–[12]. This strategy for generalizing Mie theory to provide solutions in cases of arbitrary incident beams has led to generalized Lorenz-Mie theory (GLMT). Solutions according to GLMT are of an almost identical nature to solutions according to Mie theory, but GLMT takes the shape of the incident beam into account. If the incident laser beam is centered on the scatterer to a good approiximation (if the beam is "on-axis"), then the solution for scattered intensity pattern according to GLMT takes a nearly identical form to that according to Mie theory[13]. This is not unintuitive, since the solution is the superposition of many Mie theory solutions. Consequently, the asymmetry exhibited in each of the Mie theory solutions is also present in solutions according to GLMT. In his doctoral thesis for the University of Rochester, Dr. Zachary Smith includes scattergrams produced according to both models, for light scattered by a polystyrene sphere with a diameter of 6µm, shown in figure 2.3. There are visible differences in the two scattergrams, specifically in the spacing between local irradiance maxima and in the irradiance of individal maxima, but the general features are comparable. The asymmetry on which this thesis focuses is visible to a similar degree in both, and the axes of symmetry of the two scattergrams, shown by dashed lines, are identical.

2.3.2 Literature review of angular scattering experiments

Angular light scattering has been used to obtain size estimates for and detect size changes in cell organelles. Some cellular processes and certain diseases cause organelles to swell or shrink. Detection of organelle size changes over time and estimations of organelle size have been used to diagnose and study such processes and diseases. Cancer, for example, is sometimes indicated by enlarged nuclei, and apoptosis, which is cell death according to natural processes, is indicated by changes in mitochondrial morphology. Both of these

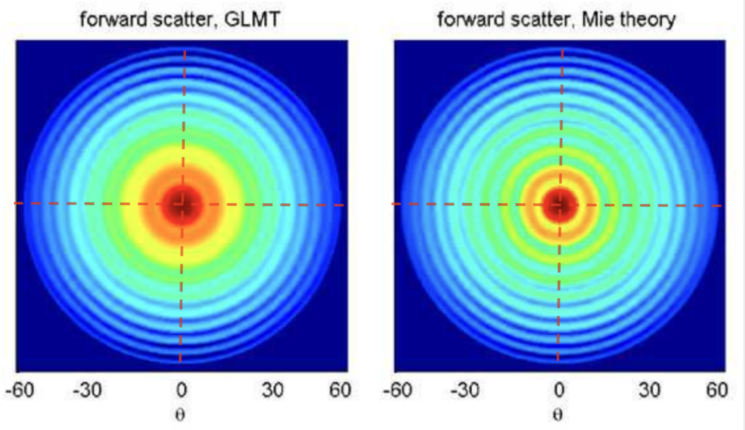

FIGURE 2.3: Simulated scattergrams for light scattered by a 6µm polystyrene bead according to GLMT (left) and Mie theory (right), originally published by Dr. Zachary Smith in his doctoral thesis for the University of Rochester[7]. Red, dashed lines have been added to show that the axes of symmetry are identical between the two.

indicators can be detected based on changes in light scattering. Raman scattering, for example, has been used to detect cancer and distinguish cancerous cells from noncancerous surrounding tissue [14]–[16].

In 2005, Wilson and Foster. measured the irradiance of light scattered at angles ranging from 5° to 90° by intact cells. This was done using a goiniometer, which detected the irradiance of scattered light as it moved along a circular path with the specimen at its center. The acquisition process took approximately two minutes. A Mie theory based model was used to simulate angular scattering by two populations of cell organelles with different mean sizes and broad size distributions. The experimental scattering data were fit to theory in order to obtain an estimate for the mean sizes of populations of organelles. Mitochondria were found to be the dominant scatterers by intact cells[17].

Using the goiniometer system and fitting to a Mie theory model, Wilson et al. were able to detect an increase in size of the organelles within

EMT6 cancer cells after they were subjected to oxidative stress (by photodynamic insult), which indicated mitochondrial swelling had occurred. Specifically, light was scattered more predominantly in the forward direction after swelling was induced and less light was scattered at small angles, which indicated an overall increase in the size of the scatterers. The scattering was also measured from isolated mitochondria and fit to a Mie theory model which assumed a single size distribution. They estimated the mean size of these mitochondria to be 0.89μm ± 0.2μm. Because the scattering from isolated mitochondria was so similar to scattering from whole cells, they concluded that mitochondrial scattering, as opposed to scattering by other organelles like the nucleus, dominates in the forward direction. They also concluded that it is feasible to monitor mitochondrial morphology using angular scattering methods[18].

In 2007, Wilson et al. used angular scattering methods to study apoptosis. In particular, they focused on the role of cytochrome c in this process and the relationship between morphological changes in mitochondria and the release of cytochrome c into the cytosol. They used immunofluorescence microscopy to monitor the subcellular location of cytochrome c while using angular scattering techniques to monitor the size of mitochondria within the cells. The angular scattering measurements were obtained using a goiniometer and size estimates were extracted by comparision to a Mie theory model. Changes in the angular scattering measurements were observed at the same time that cytochrome c was released by mitochondria into the cytosol. Based on the change in light scattering, they were able to detect a 4% overall size increase in mitochondria[19].

Cottrell, Wilson, and Foster used a modified, commercially-available inverted microscope to collect light scattered by a specimen and produce a scattergram. This was markedly different from the goiniometer based method used by Wilson et al. Rather than yielding a one-dimensional set of data points representing the irradiance of light scattered at a series of angles, collected over the course of approximately two minutes, this method allowed for the instantaneous capture of two-dimensional scattering data through an angle range of approximately 0° to 18°. They collected scattergrams from fluorescent, absorbing, polystyrene microspheres with known diameters and a narrow size distribution and compared these to a Mie theory model. They estimated the diameter of the microspheres to within less than two percent of the manufacturer's specified value[4]. To my knowledge, this group was the first to image the scattered light and produce a scattergram.

Smith and Berger constructed a system capable of collecting both Raman scattering and elastic scattering in the backward direction, producing scattergrams depicting light scattered at angles out to approximately 45° as measured from the optical axis in the backward direction. Because most of the light incident on a particle (greater by a factor of approximately 1×10^{6}, according to Smith and Berger) is scattered elastically, the signal from inelastic Raman scattering is far weaker than the signal from light scattered elastically in the backward direction. The stronger elastic scattering signal must be filtered out if the Raman signal is to be distinguished. Rather than discard the elastically backscattered light, Smith and Berger collected it with a microscope objective and extracted from it morphological information about the scatterer. It was necessary to use a focused laser with high intensity as the excitation beam so that the Raman scattering signal would be detectable. They compared the recorded angular scattering data to simulated scattergrams produced based on Mie theory and simulated scattergrams produced based on GLMT and were able to estimate the size of microspheres with a precision of 3nm. Because of the noise in their experimental data, they found that fits to GLMT and Mie theory were similar for the backscattered light[20].

Smith and Berger later published work with a slightly modified system that was capable of collecting both forward and backward scattering, from approximately 0° to 60° in the forward direction and out to approximately 60° with respect to the optical axis in the backward direction. Illumination was provided by a focused laser beam with a spot size at the specimen of approximately 7µm. They validated their system by measuring scattering from single polystyrene beads, multiple beads with a single, narrow size distribution, and multiple beads containing two differently-sized populations. They were able to distinguish between the two populations of beads and estimate the size of each population with a precision of approximately 100nm. Scattering from human immune cells, granulocytes, and lymphocytes was also measured, and estimates for the mean size of different populations of subcellular structures within multiple intact cells were extracted[5].

Smith, Chu, and Wachsmann-Hogiu created a system for recording light scattered by particles in suspension with a cell phone camera as the detector. The system was capable of collecting light scattered from approximately 3° to 15°. Scattering from suspensions of beads with three different nominal diameters was analyzed and the diameters were estimated with a precision of between 4 and 8nm. They also measured the scattering from fat and protein droplets in suspension, produced by diluting milk in water, and from baker's yeast suspended in water, and extracted size estimates from the scattering data which were consistent with existing literature. Finally, scattering from human red blood cells, which were treated with a sphering agent that caused them to transform from their natural shape into rough spheres, was measured and extracted average size estimates which were both consistent with values for a healthy donor and with estimates calculated based on conventional microscope images[21].

Cannaday et al. investigated theoretically how the size of the angle range recorded in scattergrams affects the accuracy and precision of fits to GLMT. Scattergrams were simulated based on GLMT for the cases of single populations of polystyrene beads with a narrow log-normal size distribution with mean diameters of 1µm and 5µm and for the case of a single population of cell organelles with a broad log-normal size distribution with a mean diameter of 1.3µm. The latter distribution was chosen to approximate that of cell organelles as reported by Wilson et al.[22]. Noise was added to the simulated data and designed to resemble that which was observed in experimental scattergrams. Fits were compared for scattergrams which included angles ranging from 10^o to 60^o and for scattergrams including only 20^o to 60^o. It was found that the fits for simulated bead populations had higher uncertainty when angles below 20^o were excluded. It was found that the uncertainty in fits for the simulated organelle population increased significantly when angles below 14^o were excluded. Experimental measurements were also collected using an angular scattering microscope system. The system was capable of collecting light scattered by single cells over an angle range of approximately 10^o to 60^o. Fits of experimental scattering data from 1µm and 5µm polystyrene beads and from single mouse cancer cells confirmed what was found in simulations regarding the importance of collecting angles below 20^o. The effect of these angles on the fits was found to increase as the size of the scatterer decreased[6].

Chapter 3

Azimuthal asymmetry in Mie theory and GLMT

3.1 Introduction

It will now be shown theoretically that the azimuthal asymmetry noted in Chapter 1, and with which this thesis is primarily concerned, is related to the polarization of the incident light. In his thesis, Smith derives an equation (equation 3.1 below) for the intensity of light scattered at each angle by a Mie scatterer centered at the origin, based on the work of Bohren and Huffman, which is in turn based on Mie theory[7]. The form of the scattered intensity equation according to GLMT is identical except that a linear factor is included in the sum to account for the shape of the incident beam, and the following analysis is therefore equally applicable to GLMT, as noted in Chapter 1. The relationship between the polarization and the asymmetry of the scattered intensity pattern is reflected in the scattered intensity equations, but the mathematics are difficult to interpret physically. Many of the factors in the scattered intensity equations lack a clear physical meaning and are introduced instead for mathematical convenience. For this reason, the concise scattered intensity equations must be expanded and explained, and their derivations must be summarized, if a better understanding of the asymmetry is to be gained.

3.2 The scattered intensity equation

The scattered intensity equation provided by Smith and based on Mie theory is[7]

$$I_s \propto \frac{|E_0|^2}{(kr)^2}(|S_2(\cos\theta)|^2\cos^2\phi + |S_1(\cos\theta)|^2\sin^2\phi). \tag{3.1}$$

E_0 is the amplitude of the electric field of the incident light wave, k is the wavenumber, which is related to the wavelength λ of the light according to $k = 2\pi/\lambda$, r, θ, and ϕ are the standard spherical coordinates, and S_1 and S_2 are the following sums, which are functions of $\cos\theta$ that encompass the θ dependency of the equation, and are called the scattering amplitude functions[7]:

$$S_1 = \sum_{n=1}^{\infty}\frac{2n+1}{n(n+1)}(a_n\pi_n(\cos\theta) + b_n\tau_n(\cos\theta)), \tag{3.2}$$

$$S_2 = \sum_{n=1}^{\infty}\frac{2n+1}{n(n+1)}(a_n\tau_n(\cos\theta) + b_n\pi_n(\cos\theta)). \tag{3.3}$$

The functions π_n and τ_n, dependent only on θ, are given as[7]

$$\begin{aligned} \pi_n &= \tfrac{P_n^1}{\sin\theta}, \\ \tau_n &= \tfrac{dP_n^1}{d\theta}, \end{aligned} \tag{3.4}$$

where P_n^1 is a first-order associated Legendre function of degree n. The coefficients a_n and b_n are given as[7]

$$\begin{aligned} a_n &= \tfrac{m^2 j_n(mx)[xj_n(x)]' - j_n(x)[mxj_n(mx)]'}{m_2 j_n(mx)[xh_n^{(1)}(x)]' - h_n^{(1)}(x)[mxj_n(mx)]'}, \\ b_n &= \tfrac{j_n(mx)[xj_n(x)]' - j_n(x)[mxj_n(mx)]'}{j_n(mx)[xh_n^{(1)}(x)]' - h_n^{(1)}(x)[mxj_n(mx)]'}, \end{aligned} \tag{3.5}$$

where j_n and h_n are bessel and hankel functions of order n, respectively, $m = n_1/n_2$ is the relative refractive index of the particle, n_1, as compared to that for its surrounding medium, n_2, and x is the size parameter

$$x = 2\pi n_2 a/\lambda, \tag{3.6}$$

where a is the radius of the scatterer and λ is the wavelength of the incident light.

The derivations of Smith, Bohren and Huffman, and Mie all consider the direction of propagation of the incident light to be along the z-axis (axis 3 in Mie's 1908 paper), directed into the scattergram, and the polarization of the incident light to be along the x-axis (axis 1). The polar angle θ is measured with respect to the z-axis, and the azimuthal angle ϕ is measured with respect to the x-axis[7]–[9]. This is depicted in figure 2.2 in Chapter 2.

The asymmetry exhibited in the theoretical scattergrams is azimuthal and therefore related to the azimuthal angle ϕ. Equation 3.1 contains numerous θ dependencies, but the variable ϕ is seen only twice, within sine-squared and cosine-squared functions. The other factors which constitute the amplitudes of these functions will be discussed in Section 3.4. The two functions, plotted over two periods in Figure 3.1, oscillate between the values of zero and one, depending on the azimuthal angle ϕ, and are exactly 90^o out of phase with each other. When the sine-sqared function is equal to zero, the cosine-squared function is equal to one, and vice versa. As ϕ increases, the two terms in equation 3.1 oscillate between zero and their maximum value. At $\phi = 0, 180^o$, the sine-squared term vanishes, and the cosine-squared term determines the intensity at each θ. At $\phi = 90, 270^o$, the cosine-squared term vanishes. In between these values of ϕ, both terms contribute to determine the scattering features.

The amplitude of the cosine-squared term includes the sum S_1 and the

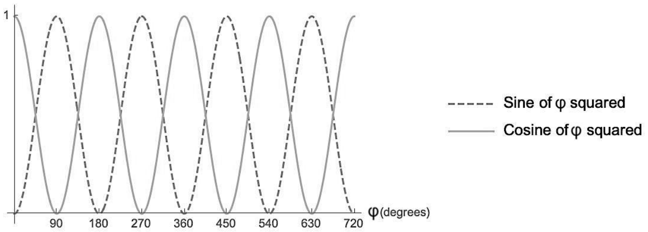

FIGURE 3.1: Sine of ϕ squared and cosine of ϕ squared, plotted over two periods. The two functions oscillate between zero and one and are exactly 90^o out of phase with each other.

amplitude of the sine-squared term includes the sum S_2. These sums are the same except for the fact that the size-dependent coefficients are applied to different scattering amplitude functions. The scattering amplitude functions (3.4), which oscillate as θ varies, produce the characteristic irradiance maxima and minima seen in scattergrams. If the two scattering amplitude functions are different, then the features of the scattergram, such as ripple spacing, change with ϕ. Accordingly, the axes of symmetry for the theoretical intensity pattern are directed along $\phi = 0, 180^o$ and $\phi = 90, 270^o$. If the two sums are not different, then the scattergram does not exhibit asymmetry, since the features of the scattergram do not change with ϕ.

3.3 Mathematical source of asymmetry

Bohren and Huffman provide a rigorous account of the Mie theory derivation from which equation 3.1 was adapted. The first and most challenging step is to model the excitation beam, a linearly-polarized plane wave, in a way that conforms to the spherical symmetry of the problem. The use of the spherical coordinates, r, θ and ϕ, is therefore expedient. The plane wave is written as[9],

$$\vec{E}_i = E_0 e^{ikr\cos\theta} \hat{e}_x, \tag{3.7}$$

where E_0 is the maximum amplitude of the electric field. Crucially, the unit vector $\hat{e}_x$ indicates that the wave's polarization is in the x-direction, and can be expanded as follows to conform to a spherical coordinate system[9],

$$\hat{e}_x = \sin\theta\cos\phi\hat{e}_r + \cos\theta\cos\phi\hat{e}_\theta + \sin\phi\hat{e}_\phi. \tag{3.8}$$

3.3.1 Spherical vector harmonics

The plane wave in equation 3.7 is then represented by the superposition of spherical vector harmonics as will be explained. These harmonics must satisfy the vector wave equation if they are to represent a physically-realizable plane wave. Bohren and Huffman simplify the process for fulfilling this criterion by constructing a vector function,

$$\vec{M} = \nabla \times (\vec{r}\psi), \tag{3.9}$$

which has zero divergence and includes the scalar function ψ, which is a solution to the scalar wave equation, as discussed below. The vector $\vec{r}$ is the radius vector in spherical polar coordinates. It is clear that $\vec{M}$ has zero divergence because

$$\nabla \cdot (\nabla \times \vec{A}) = 0 \tag{3.10}$$

for any vector $\vec{A}$[7]. This is important because $\vec{M}$ will eventually be used to represent an electric field, and, according to Maxwell's equations, electric and magnetic fields have zero divergence in areas where there is no net electric charge. By use of vector identities, it is true that[9]

$$\nabla^2\vec{M} + k^2\vec{M} = \nabla \times [\vec{r}(\nabla^2\psi + k^2\psi)]. \tag{3.11}$$

Therefore, if ψ satisfies the scalar wave equation,

$$\nabla^2 \psi + k^2 \psi = 0, \tag{3.12}$$

then $\vec{M}$ satisfies the vector wave equation,

$$\nabla^2 \vec{M} + k^2 \vec{M} = 0, \tag{3.13}$$

as well[9]. The vector $\vec{r}$ is perpendicular to $\vec{M}$, which is important, since the former will be used to represent the direction of propagation of the incident plane wave, and the latter will be used to represent its electric and magnetic fields. Furthermore, Bohren and Huffman define

$$\vec{N} = \frac{\nabla \times \vec{M}}{k}, \tag{3.14}$$

which also has zero divergence by equation 3.10 and also satisfies the vector wave equation by equation 3.11. Lastly, since $\nabla \times \vec{N} = k\vec{M}$, $\vec{M}$ and $\vec{N}$ have all of the necessary properties to represent an electric field. Note that, on their own, neither $\vec{M}$ nor $\vec{N}$ necessarily represents an electric or magnetic field. Since $\vec{M}$ and $\vec{N}$ will satisfy the vector wave equation if ψ satisfies the scalar wave equation, ψ may be used to generate the spherical vector harmonics.

The first step to solving the scalar wave equation for ψ is to assume that a solution exists of the form $\psi(r, \theta, \phi) = R(r)\Theta(\theta)\Phi(\phi)$, constituted of functions dependent on only one variable. This strategy for solving differential equations is called *separation of variables*. The three separated equations of one variable may then be solved individually[9],

$$\frac{d^2\Phi}{d\phi^2} + m^2\Phi = 0, \tag{3.15}$$

$$\frac{1}{\sin\theta}\frac{d}{d\theta}\left(\sin\theta\frac{d\Theta}{d\theta}\right)+\left[n(n+1)-\frac{m^2}{\sin^2\theta}\right]\Theta=0, \tag{3.16}$$

$$\frac{d}{dr}\left(r^2\frac{dR}{dr}\right)+\left[k^2r^2-n(n+1)\right]R=0. \tag{3.17}$$

First, consider equation 3.15. Two solutions are required because if, for a given integer m, Φ_m is a solution to 3.15, then $\Phi_{(-m)}$, for a negative integer, is not a linearly independent solution[9]. There are, then, two linearly independent solutions,

$$\Phi_e=\cos m\phi, \Phi_o=\sin m\phi, \tag{3.18}$$

where the subscripts e and o indicate even and odd[9]. Here we have the first appearance of the crucial functions sine and cosine of ϕ.

The solutions to 3.16 in the present case must be finite at $\theta=0,\pi$, and we therefore choose Legendre functions of the first kind in $\cos\theta$, $P_n^m(\cos\theta)$, of degree n and order m. Solutions to 3.17 are spherical Bessel functions or a linear combination of these functions, such as Hankel functions.

The requirement for two linearly independent solutions to Φ leads to two solutions to ψ,

$$\psi_{emn}=\cos m\phi P_n^m(\cos\theta)z_n(kr), \tag{3.19}$$

$$\psi_{omn}=\sin m\phi P_n^m(\cos\theta)z_n(kr), \tag{3.20}$$

where P_n^m are Legendre functions of the first kind in $\cos\theta$ of degree n and order m, n is an integer such that $n=m,m+1,m+2\ldots$, k is the constant from the scalar wave equation, and z_n is any one of four spherical Bessel functions, $j_n, y_n, h_n^{(1)}$, or $h_n^{(2)}$[9]. Which of these functions are chosen is discussed below.

These solutions may be inserted into equations 3.9 and 3.14 to construct the desired spherical vector harmonics, written in component form as[9]

$$\begin{aligned}\vec{M}_{emn} = & \frac{-m}{\sin\theta}\sin m\phi P_n^m(\cos\theta) z_n(\rho)\hat{e}_\theta \\ & - \cos m\phi \frac{dP_n^m(\cos\theta)}{d\theta} z_n(\rho)\hat{e}_\phi, \end{aligned} \tag{3.21}$$

$$\begin{aligned}\vec{M}_{omn} = & \frac{m}{\sin\theta}\cos m\phi P_n^m(\cos\theta) z_n(\rho)\hat{e}_\theta \\ & - \sin m\phi \frac{dP_n^m(\cos\theta)}{d\theta} z_n(\rho)\hat{e}_\phi, \end{aligned} \tag{3.22}$$

$$\begin{aligned}\vec{N}_{emn} = & \frac{z_n(\rho)}{\rho}\cos m\phi n(n+1) P_n^m(\cos\theta)\hat{e}_r \\ & + \cos m\phi \frac{dP_n^m(\cos\theta)}{d\theta}\frac{1}{\rho}\frac{d}{d\rho}[\rho z_n(\rho)]\hat{e}_\theta \\ & -m \sin m\phi \frac{P_n^m(\cos\theta)}{\sin\theta}\frac{1}{\rho}\frac{d}{d\rho}[\rho z_n(\rho)]\hat{e}_\phi, \end{aligned} \tag{3.23}$$

$$\begin{aligned}\vec{N}_{omn} = & \frac{z_n(\rho)}{\rho}\sin m\phi n(n+1) P_n^m(\cos\theta)\hat{e}_r \\ & + \sin m\phi \frac{dP_n^m(\cos\theta)}{d\theta}\frac{1}{\rho}\frac{d}{d\rho}[\rho z_n(\rho)]\hat{e}_\theta \\ & +m \cos m\phi \frac{P_n^m(\cos\theta)}{\sin\theta}\frac{1}{\rho}\frac{d}{d\rho}[\rho z_n(\rho)]\hat{e}_\phi. \end{aligned} \tag{3.24}$$

3.3.2 Expansion of plane wave

The spherical vector harmonics (equations 3.21 through 3.24) can then be used to represent equation 3.7, the incident plane wave. They will each be superposed in the appropriate proportions according to an infinite double-sum,

$$\vec{E}_i = \sum_{m=0}^{\infty} \sum_{n=m}^{\infty} (B_{emn}\vec{M}_{emn} + B_{omn}\vec{M}_{omn} + \\ A_{emn}\vec{N}_{emn} + A_{omn}\vec{N}_{omn}), \tag{3.25}$$

where A_{-mn} and B_{-mn} are coefficients dictating the degree to which each spherical vector harmonic contributes to the model of the plane wave.

Bohren and Huffman prove through a rigorous process that all of the spherical vector harmonics are orthogonal to each other[9]. From this, it follows that the coefficients in the above sum take the forms,

$$B_{emn} = \frac{\int_0^{2\pi} \int_0^{\pi} \vec{E}_i \cdot \vec{M}_{emn} \sin\theta d\theta d\phi}{\int_0^{2\pi} \int_0^{\pi} |\vec{M}_{emn}|^2 \sin\theta d\theta d\phi}, \tag{3.26}$$

$$B_{omn} = \frac{\int_0^{2\pi} \int_0^{\pi} \vec{E}_i \cdot \vec{M}_{omn} \sin\theta d\theta d\phi}{\int_0^{2\pi} \int_0^{\pi} |\vec{M}_{omn}|^2 \sin\theta d\theta d\phi}, \tag{3.27}$$

$$A_{emn} = \frac{\int_0^{2\pi} \int_0^{\pi} \vec{E}_i \cdot \vec{N}_{emn} \sin\theta d\theta d\phi}{\int_0^{2\pi} \int_0^{\pi} |\vec{N}_{emn}|^2 \sin\theta d\theta d\phi}, \tag{3.28}$$

$$A_{omn} = \frac{\int_0^{2\pi} \int_0^{\pi} \vec{E}_i \cdot \vec{N}_{omn} \sin\theta d\theta d\phi}{\int_0^{2\pi} \int_0^{\pi} |\vec{N}_{omn}|^2 \sin\theta d\theta d\phi}. \tag{3.29}$$

3.3.3 Polarization

It is now necessary to consider the polarization of the incident light. First, note that sine and cosine are orthogonal functions in the sense that

$$\int_{x=0}^{2\pi} W \sin px \cos qx dx = 0 \tag{3.30}$$

for any function W which is not dependent on x and for any integers p and q. Remember now the unit vector in equation 3.8. In the x-polarized case, the dot products in the coefficients between $\vec{E}_i$ and $\vec{M}_{emn}$ and between $\vec{E}_i$ and $\vec{N}_{omn}$, in equations 3.26 and 3.29 respectively, include an expression of the form $\sin p\phi \cos q\phi$ in each term. Since all of these terms are integrated with respect to ϕ from 0 to 2π, it follows from equation 3.30 that $B_{emn} = A_{omn} = 0$ for all m and n. The other two coefficients are also zero unless $m = 1$[9]. Furthermore, because the incident field is finite at the origin, $j_n(kr)$, the only one of the four bessel functions mentioned above which is well-behaved at the origin, must be used in the generating functions ψ_{o1n} and ψ_{e1n}; this is indicated by the superscript (1). The expansion for $\vec{E}_i$ therefore takes the form[9]

$$\vec{E}_i = E_0 \sum_{n=1}^{\infty} \left(B_{o1n}\vec{M}_{o1n}^{(1)} + A_{e1n}\vec{N}_{e1n}^{(1)}\right). \tag{3.31}$$

3.3.4 The scattered electric field

When the incident beam reaches the surface of the scatterer, the properties of the medium through which the beam propagates change abruptly, over a thickness of atomic dimensions. Therefore, on a relatively macroscopic level, there is a discontinuity of the electric and magnetic fields at the surface of the scatterer. However, the tangential components of both fields must be continuous at this boundary. We may express this through the following boundary condition,

$$(\vec{E}_i + \vec{E}_s - \vec{E}_l) \times \vec{e}_r = (\vec{H}_i + \vec{H}_s - \vec{H}_l) \times \vec{e}_r = 0, \tag{3.32}$$

where $\vec{E}$ and $\vec{H}$ are the electric and magnetic fields, respectively, and the subscripts i, s, and l denote the incident, scattered, and internal fields, respectively. Equation 3.32 is derived from the principle of conservation of energy, as is described by Bohren and Huffman[9].

Based on 3.32, the orthogonality of the vector harmonics, and the form of the series expansion of the incident field (equation 3.31), the expansion for the scattered field may be written as

$$\vec{E}_s = \sum_{n=1}^{\infty} E_n \big(i a_n \vec{N}_{e1n}^{(3)} - b_n \vec{M}_{o1n}^{(3)} \big). \tag{3.33}$$

Here, $E_n = i^n E_0 (2n+1)/n(n+1)$ and a_n and b_n are given in equation 3.5. The spherical Hankel function $h_n^{(1)}$ is chosen, denoted by the superscript (3) on each vector harmonic, in this expansion because both of the Bessel functions, j_n and y_n, which are both included in the spherical Hankel functions, are well-behaved in the region outside of the scatterer. Furthermore, $h_n^{(2)}$ was rejected because, as Bohren and Huffman explain, it corresponds to an incoming wave, in contrast to $h_n^{(1)}$, which corresponds to an outgoing wave. The scattered field is almost entirely an outgoing wave at distances far from the scatterer.

At distances far from the scatterer, the radial component of N_{e1n} in equation 3.33 is negligible, which is consistent with the fact that, as Bohren and Huffman note, the scattered electric field at such distances is almost entirely transverse[1][9]. Equation 3.33 can be resolved into its transverse components as follows,

$$E_{s\theta} \sim E_0 \frac{e^{ikr}}{-ikr} \cos\phi S_2(\cos\theta), \tag{3.34}$$

$$E_{s\phi} \sim E_0 \frac{e^{ikr}}{-ikr} \sin\phi S_1(\cos\theta), \tag{3.35}$$

where S_1 and S_2 are the sums given in equations 3.2 and 3.3. The two transverse components, which are orthogonal to each other, add in quadrature to yield the magnitude of the scattered electric field, and the intensity of this field is proportional to the square of the amplitude. Hence, we arrive at the

---

[1] A transverse electric field is one which oscillates in a plane perpendicular to the direction of the field's propagation.

scattered intensity, given in equation 3.1.

The sine and cosine functions of ϕ appear in equation 3.1 because they are in equations 3.34 and 3.35, the transverse components of the scattered electric field. Their presence in these components may be traced back to the corresponding components of the spherical vector harmonics in equation 3.33, the scattered field expansion. These particular vector harmonics appear in the expansion because they are in the expansion for the incident plane wave, and these particular vector harmonics are present in the plane wave expansion because of the polarization of the incident beam, which was explained in subsection 3.3.3.

If the incident beam is a y-polarized plane wave, meaning that its electric field oscillates along the y-axis, $\hat{e}_x$ in equation 3.7 is replaced by

$$\hat{e}_y = \sin\theta \sin\phi \hat{e}_r + \cos\theta \sin\phi \hat{e}_\theta + \cos\phi \hat{e}_\phi, \tag{3.36}$$

in which, compared to $\hat{e}_x$, every instance of $\sin\phi$ has been replaced with $\cos\phi$ and vice versa. The result is that $\vec{M}_{omn}$ and $\vec{N}_{emn}$ in equation 3.25 vanish instead of their even and odd counterparts. Therefore, as Bohren and Huffman note[9],

$$\vec{E}_s(\phi; \text{x-polarized}) = \vec{E}_s(\phi + \frac{\pi}{2}; \text{y-polarized}), \tag{3.37}$$

the scattered field resulting from a y-polarized incident beam is the same as that resulting from an x-polarized incident beam, except that it is shifted in ϕ by $\pi/2\text{rad} = 90^{\text{o}}$. This amounts to a 90^{o} rotation of the scattering pattern. This is somewhat intuitive, since Bohren and Huffman also note that

$$\begin{aligned} \vec{M}_{o1n}(\phi) &= \vec{M}_{e1n}(\phi + \frac{\pi}{2}); \\ \vec{N}_{o1n}(\phi) &= \vec{N}_{e1n}(\phi + \frac{\pi}{2}). \end{aligned} \tag{3.38}$$

It has now been shown that the sine and cosine squared of ϕ functions which make azimuthal asymmetry mathematically possible are related to the polarization in that they result from the conversion of the cartesian unit vector $\vec{e}_x$, which specifies the polarization of the incident plane wave, into spherical coordinates.

3.3.5 Physical interpretation

Bohren and Huffman note that the scattered electric field is almost entirely transverse at distances far from the scatterer[9]. The scattered light at this distance all has the same polarization as the incident light, which is x-polarized in the case of equation 3.1. In a cartesian coordinate system, then, the scattered electric field at any point has only one component, directed along $\hat{e}_x$. The representation of the scattered field in spherical coordinates, however, is deceptive because in this coordinate system the direction of each unit vector varies. Therefore, even though the direction of the scattered electric field is constant relative to the optical axis, it is not constant relative to the spherical unit vectors. In short, the use of a spherical coordinate system with unit vectors with varying directions leads to an equation which is more complicated than the physical situation represented by it would seem to suggest.

3.4 The two sums

It has been explained that the asymmetry is mathematically possible because of the two trigonometric functions which are mutually out of phase. However, it remains to be explained how the two sums, S_1 and S_2, come to be different, for this difference is a necessary condition for an azimuthally asymmetrical intensity pattern. The sums themselves are simply the consolidation of all θ dependencies in the expression for the scattered field, and these dependencies may be traced back to the spherical vector harmonics. The sums are each included in the amplitude for one of the transverse components of the scattered field, and they are the combination of like components of the two spherical vector harmonics in equation 3.31. They differ because these individual components of the spherical vector harmonics differ. The vector harmonics were constructed by taking the curl of a solution to the scalar wave equation, ψ_{omn} or ψ_{emn}. Each component in the curl includes a partial derivative of ψ_{-mn} with respect to a different variable, and the result of this is that all three components are distinct. The curl of ψ_{omn} or ψ_{emn} was evaluated to obtain $\vec{M}_{-mn}$, and subsequently the curl of the result was evaluated to obtain $\vec{N}_{-mn}$. These curls were evaluated in an effort to ensure that the spherical vector harmonics satisfied Maxwell's equations, which must necessarily be satisfied if a mathematical model is to represent physical electromagnetic phenomena. Any further explanation would require an exploration into why Maxwell's equations are what they are, and that is beyond the scope of this thesis.

Chapter 4

The effects of changes in polarization on experimental scattergrams

4.1 Introduction

It has been shown that the polarization of the incident light is related to the azimuthal asymmetry of theoretical Mie scattering. Furthermore, it has been shown that the axes of reflective symmetry in theoretical scattering patterns rotate with the axis of polarization. It will now be demonstrated experimentally that rotating the polarization of the incident light causes a rotation in the scattered intensity pattern. To my knowledge, this is the first time experimental demonstrations have been documented of how the polarization of incident light affects Mie scattering.

4.2 Experimental Methods

The angular scattering microscope used for the following experiments was constructed by myself and James Hoelle of Rollins College, under the supervision of Dr. Ashley Cannaday, as part of ongoing research for the Student-Faculty Collaborative Scholarship program. A diagram of the microscope used for this thesis is shown in figure 4.1. The microscope includes both sample imaging and scattered light imaging modalities, which can be used simultaneously. The illumination source is a 150mW diode-pump solid state (DPSS) laser with peak output wavelength of 532nm. A half-wave plate (HWP) is mounted in a rotating mount and placed directly in front of the laser aperture so that the polarization state of the excitation beam can be altered. A linear polarizer (LP), also in a rotating mount, is mounted directly after the HWP. Following the polarizer, two lenses are used to expand the beam size and a third is used to focus it down onto the core of a polarization-maintaining, single-mode, optical fiber. The beam is expanded before the condensing lens because the minimum possible spot size for a Gaussian beam decreases as the initial beam diameter increases[1]. The beam is condensed so that the spot fits within the core of the fiber, maximizing the intensity of light transmitted through the fiber. The output end of the fiber is mounted to a vertical cage system. Upon exiting the fiber, the diverging laser light is collimated using an anti-reflective (AR) coated, plano-convex lens, L1, with a focal length of 35mm, which is placed approximately one focal length from the fiber tip. The collimated beam is focused by an AR coated, 75mm focal length, plano-convex lens, L2, to a beamwaist of $w_0 \approx 7.5\mu m$, resulting in an excitation spot with a diameter of approximately 15µm at the scatterer. The beam is condensed so that one specimen at a time can be illuminated and the scattering from a single specimen recorded. An XY translation stage is placed below the converging lens, at the focal point of the lens, to hold a sample chamber containing the specimens. The translation stage allows for gradual scanning of a sample so that an individual specimen can be positioned within the excitation spot.

An Attofluor cell chamber holding a round coverslip sits atop the translation stage. For the experiments outlined in this thesis, polystyrene beads with narrow size distributions were diluted in twice-distilled water, and a

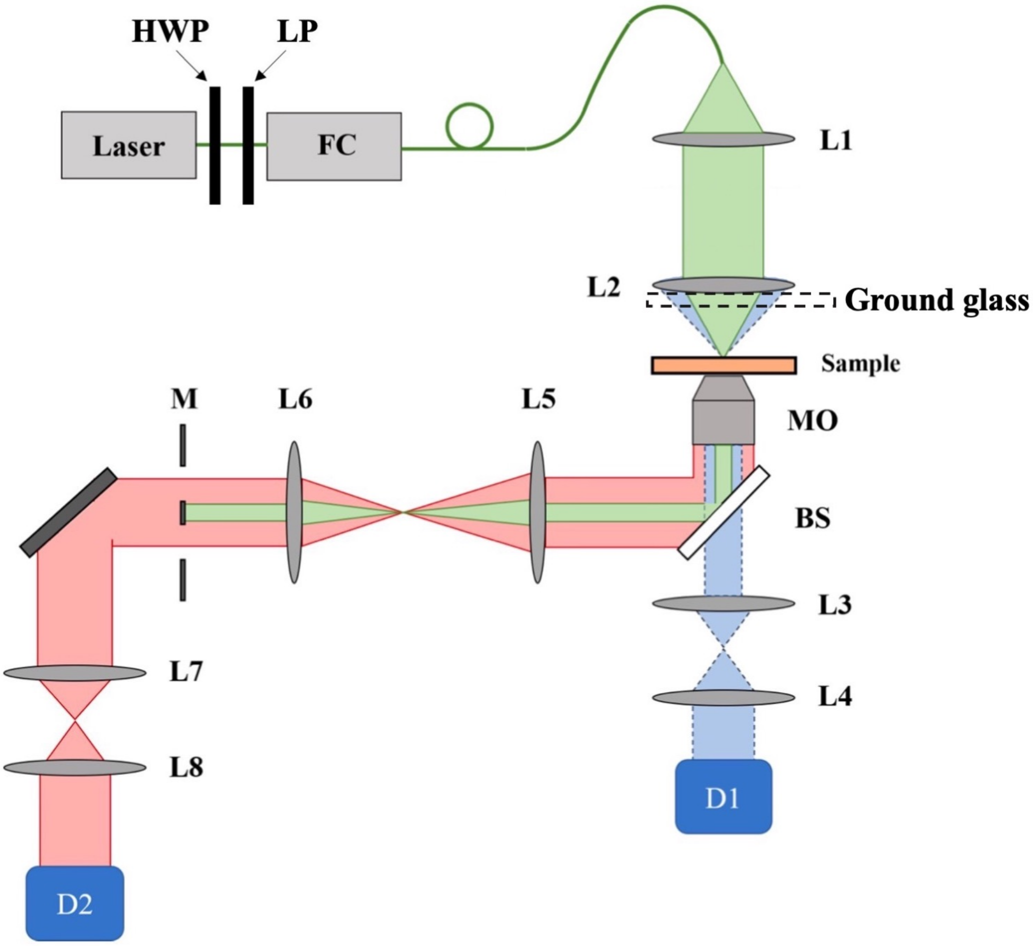

FIGURE 4.1: Diagram of the optical system used to collect scattering data for this thesis[23]. The system consisted of: A laser; a half-wave plate, HWP; a linear polarizer, LP; an optical fiber; a fiber coupling system, FC; converging lenses, L1-L8; a microscope objective, MO; a beamsplitter, BS; CMOS detectors, D1 and D2; a mask, M. The green path represents the excitation beam, the red path shows the scattered light imaging modality, and the blue path shows the sample imaging modality. A piece of ground glass could be inserted after L2 in order to produce an approximately uniform illumination field for the sample imaging modality.

small amount of the resulting suspension was transferred into the cell chamber. The water was allowed to evaporate overnight so that the beads adhered electrostatically to the coverslip. Samples were prepared using one of two sizes of beads. The two sizes of beads had nominal diameters of 1.75µm and 5µm. The manufacturer-specified size distribution of the 1.75µm beads was

1.745μm ± 0.022μm and that for the 5μm beads was 5.027μm ± 0.047μm.

An achromatic, 100x, oil-immersion microscope objective (MO) with a numerical aperture (NA) of 1.25 is placed below the sample plane in an XYZ translation stage to collect the forward-scattered light from the specimen. The high NA allows for collection of light over a large angle range of approximately 0° to 60°. A 50/50 plate beamsplitter (BS) directs the light collected by the objective along two paths. Light transmitted through BS is incident on L3, which acts as an eyepiece for the MO, forming a microscope. L4 is used to image the sample plane onto a complementary metal-oxide-semiconductor (CMOS) detector. When a piece of ground glass is placed after L2 such that the illumination by the laser at the sample plane is approximately uniform and extends over a large area, this portion of the system records an image of the sample plane, so that a bead can be located and positioned at the center of the excitation spot by use of the XY translation stage. With the ground glass removed, the excitation spot can be seen in relation to any beads present in the frame, allowing for an isolated bead to be placed precisely at the center of the excitation spot. With a bead so positioned, light from the excitation spot is elastically scattered by the bead, and this light is collected by the microscope objective.

Along the path of light reflected by the beamsplitter, a 4f system[1] consisting of two lenses, L5 and L6, with focal lengths of 300mm and 250mm respectively, is used to image the scattered light collected by the microscope objective. L5 is placed so that its front focal plane aligns with the back focal plane of the microscope objective, which is the Fourier plane at which an image of the scattered light exists. A mask, consisting of a small drop of black,

---

[1] A 4f system consists of two lenses with focal lengths f_1 and f_2. The input plane is a distance f_1 to the left of the first lens, and the output plane is a distance f_2 to the right of the second lens. The two lenses are spaced so that their focal lengths align at what is called the Fourier plane[24].

acrylic paint on a microscope coverslip[2], is placed at the output plane of the first 4f system so that it is in the same plane as the image of the scattered light. The mask blocks unscattered light, at angles less than approximately 8^{o}, from proceeding through the system. Unscattered light is far more intense than the light which is elastically scattered by the bead, especially at higher scattering angles, and would produce artifacts in the image of the scattered light recorded by the second CMOS detector (D2) if not obstructed by the mask. Preventing unscattered light from reaching the detector also leaves more of the detector's dynamic range available for recording the lower-intensity scattered light. A second 4f system, consisting of two lenses, L7 and L8, with focal lengths of 50mm and 100mm respectively, is used to relay the masked image at the output plane of the first 4f system to D2, which records a final image of the scattered light. The magnification by the first 4f system is 1.2, and the magnification of the second 4f system is 2, resulting in a total magnification of 2.4.

4.2.1 Half-wave Plates

The HWP could be used to rotate the polarization of the laser light of the excitation beam. As stated in Chapter 2, the polarization of a light wave is defined by the direction in which its electric field oscillates. A HWP has two orthogonal axes which lie in its plane and is made of material which has a different refractive index, n, for electric fields or components of them which oscillate along one axis than for those which oscillate along the orthogonal one. Since the velocity, v, at which an electromagnetic wave propagates is given by $v = nc$, where c is the speed of light *in vacuo*, the component

---

[2] The paint was applied to the coverslip using the tip of a pin. The droplet of paint on the end of the pin was carefully allowed to contact the coverslip for a brief instant, so that a very small amount of paint adhered. It was difficult to control the amount of paint applied, but through a process of trial and error a droplet which was nearly circular and approximately one-half millimeter in diameter was applied, and this resulted in a mask with the desired properties.

of light's electric field which oscillates along one axis travels at a different speed through the HWP than the component oscillating along the orthogonal axis. A HWP therefore has a "fast" axis and a "slow" axis, as shown in figure 4.2. The component of the electric field of light which oscillates along the slow axis is delayed by a half-integral multiple of its wavelength compared to the component of the field which oscillates along the fast axis upon passing through the plate[3]. In the case where an electric field is polarized at an angle θ with respect to the slow axis of the HWP, as shown in figure 4.2, only one of the components of the electric field is delayed by the HWP, and the effect is to rotate the polarization through an angle of 2θ.

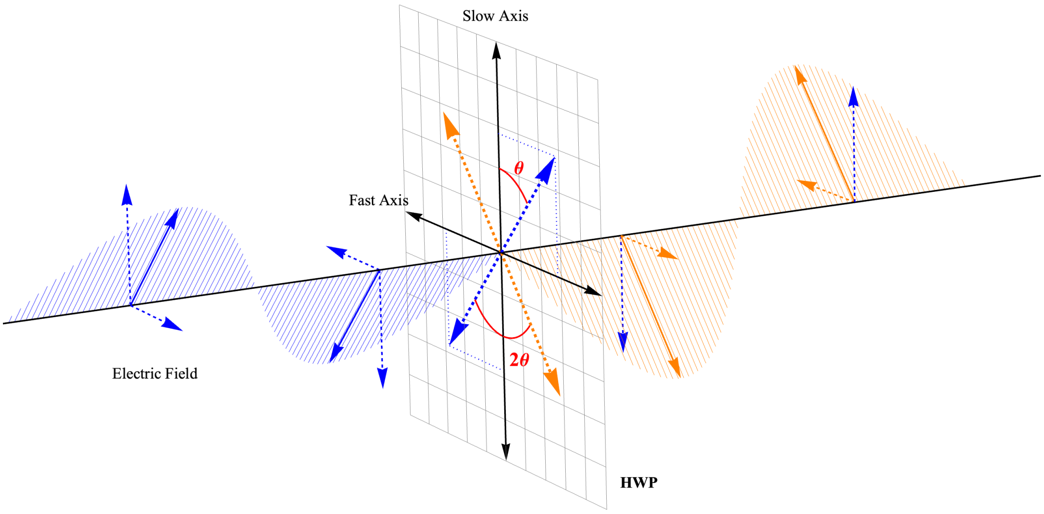

FIGURE 4.2: When the incident electric field is polarized at an angle θ with respect to the slow axis of a HWP, it can be considered in terms of its components as projected onto the axes of the HWP. Upon passing through the HWP, the component along the slow axis is delayed with respect to the component along the fast axis. The effect is to rotate the polarization axis through an angle of 2θ. The electric field is shown in blue before passing through the HWP and in orange after passing through the plate. The delayed component in the figure remains blue in color after passing through the HWP.

---

[3] The index of refraction along both axes and the thickness of the wave plate are both considered by the manufacturer, and the thickness of the wave plate is carefully controlled so as to result in the proper difference in optical path length.

4.2.2 Changing the polarization

The scattering of light by polystyrene beads was measured using the angular scattering microscope described above, and measurements were taken with the incident beam in different linear polarization states. The polarization was changed by rotating the HWP and the linear polarizer. Laser light is, in general, fully linearly polarized to a good degree. However, the polarizer was placed in the system to assure that the light was fully linearly polarized. Initially, the HWP was removed from the system and the polarizer was rotated so that its transmission axis was aligned with the polarization of the laser light, as judged by which orientation yielded the highest transmitted irradiance. The transmitted irradiance was measured in real time by the CMOS detector. The HWP was then placed before the polarizer, and the HWP was rotated until the irradiance of light transmitted through the polarizer was maximized. This maximal transmission indicated that the HWP was not altering the polarization state of the laser light. The initial orientations of the polarizer and the HWP were noted.

When the HWP was rotated by an angle θ, the polarizer was rotated by an angle of 2θ in the same direction, so that its transmission axis was aligned with the desired polarization. In the case of this experiment, three different polarization states were used. The first was the default state of the laser beam. The second was produced by rotating the HWP by $22.5^o \pm 1.00^o$, and the polarizer was rotated accordingly by $45.0^o \pm 2.00^o$. The third was produced by rotating the HWP further to an angular displacement of $45.0^o \pm 1.00^o$, and the LP was rotated accordingly to a displacement of $90.0^o \pm 2.00^o$.

4.3 Experimental measurements of angular scattering

The visible light modality of the microscope was used to locate a bead as the sample was scanned using the translation stage. Once an isolated bead was found (isolated insofar as no other beads were within a radius of approximately 25µm), the ground glass was removed and the bead was centered in the excitation spot. A visible light image of a polystyrene bead with a diameter of approximately 5µm, centered within the excitation spot, is shown in figure 4.3.

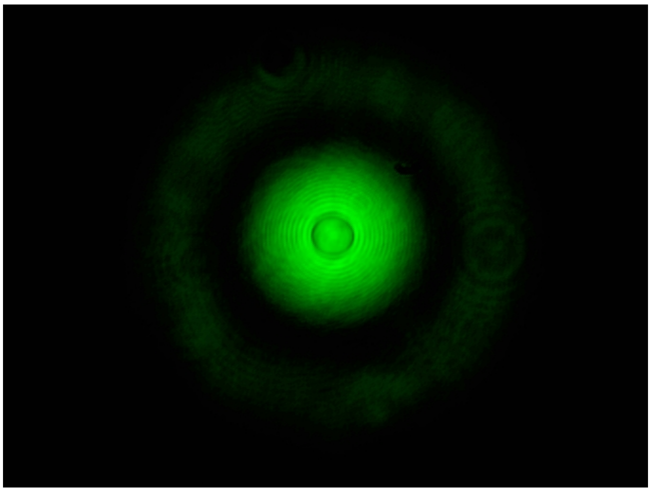

FIGURE 4.3: A bead with a diameter of approximately 5µm, centered within the excitation spot. The excitation spot had a diameter of approximately 15µm. Care was taken to ensure that no other scatterers were within a radius of 25µm from the scatterer.

Light scattered by the bead was then recorded using the scattering modality of the microscope. With the same bead centered in the excitation spot, the HWP was rotated by 22.5° ± 1.00° and the polarizer was rotated by 45.0° ± 2.00°, as described in Section 4.2.2, and the scattering was recorded. The HWP was then rotated by another 22.5° ± 1.00° and the polarizer was rotated by 45.0° ± 2.00°, and scattering from the same bead was recorded. Once the scattering of light with three different polarization states was recorded, the sample was scanned using the translation stage until another isolated bead was found. This bead was centered within the excitation spot and the process was repeated. The scattering was recorded from a total of 16 beads for each of the two sizes, 1.75µm and 5.00µm. For each of the 32 beads, scattering of light with each of the three polarization states was recorded.

Scattergrams from two beads, one of each size, and for an incident beam with each of the three polarization states, are shown in figure 4.4. The scattergrams are visibly asymmetrical, as is predicted by Mie theory and GLMT, and all exhibit approximate mirror symmetry along two orthogonal axes. Furthermore, the axes of symmetry are visibly rotated for different polarization states. The scattergrams were not rotated after being recorded.

The asymmetry of the scattering is manifested in a number of features of the scattergrams. The irradiance decreases more between maxima in two quadrants of the scattergrams than in the other two. This is more easily seen in scattergrams from 5.00µm beads than in those from the smaller beads. The effect is also more pronounced at higher angles than at angles below approximately 35°. This is likely why there is no obvious asymmetry in the scattergram published by Cottrell, et al., discussed in Chapter 1. The observations above hold true for all of the scattergrams recorded, as all of them varied in nearly identical ways when the polarization of the incident light was changed.

The linear polarizer was rotated by 45° ± 2° between recording scattergrams in the first column of figure 4.4 and recording those in the second, and the orientations of the axes of symmetry were expected to rotate by the same angle. However, the axes of symmetry of scattergrams in the first column appear to differ in their orientations from those of scattergrams in the second column by less than 25° for the 5.00µm beads and less than 31° for the 1.75µm beads. Potential reasons for this discrepancy will be discussed in Section 4.5.

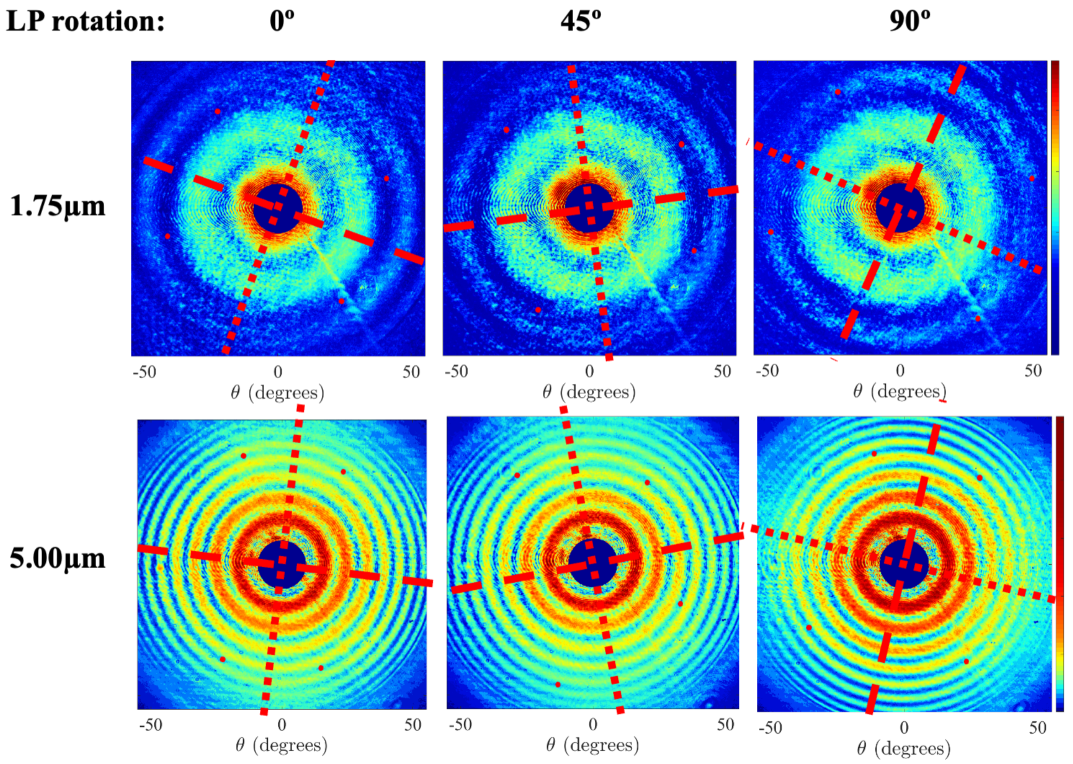

FIGURE 4.4: Scattergrams from the same 5.00µm bead (top) and the same 1.75µm bead (bottom). The leftmost scattergrams were collected with the linear polarizer (LP) in its initial state, the middle scattergrams were collected when the LP was at an angular displacement of 45°, and the rightmost scattergrams were collected when the LP was at a displacement of 90°. A colormap was added to each scattergram in MATLAB; dark blue indicates the lowest irradiance and crimson indicates the highest. The scattergrams from 1.75µm beads are plotted with a logarithmic scale for clarity. The axes of reflective symmetry are indicated by dashed, red lines, and are visibly rotated for different polarization states. Red dots indicate points at which features of the scattergram change, which were used for reference when placing the axes.

4.4 Effects of polarization on size estimates

Extracting size estimates from angular scattering data typically involves fitting experimental scattergrams to theoretical scattergrams, generated using either Mie theory or GLMT. If the assumed polarization state for the excitation beam when generating theoretical scattergrams is different from the polarization state of the experimental excitation beam, the difference in orientation between the experimental and theoretical scattergrams could potentially lead to decreased accuracy and increased uncertainty for the fits. The scattergrams collected as described in Section 4.3 were fit to theory in order to test whether rotating the polarization of the excitation beam results in improved fits to theory or changes in the mean or standard deviation of size estimates.

The scattering angle associated with each pixel on the CMOS array was determined using a diffraction grating. L2 was removed from the system so that the light incident on the translation stage was collimated, and a transmission diffraction grating with a known groove spacing was placed on the translation stage, with the grooved side facing the MO. A diffraction grating causes light to be redirected at various angles, forming a diffraction pattern with local irradiance maxima occurring at known angles, as shown in figure 4.5.

Irradiance maxima in a diffraction pattern are identified by their order, m. The central maximum is called the zeroth order maximum ($m = 0$), and corresponds to light which is undeviated after passing through the grating. The pair of maxima closest to the zeroth order on either side is a pair of first order maxima ($m = 1$), and the order increases in like manner for each pair of maxima further from the center. The angle θ at which each order occurs is dependent on the wavelength of the incident light, λ, and the distance between grooves in the grating, a, according to the diffraction grating equation[1],

$$m\lambda = a \sin\theta. \tag{4.1}$$

When the laser light, collimated by L1, was incident on the grating, it was redirected at various angles and collected by the MO in the same way as light scattered at various angles by a specimen. The diffracted orders appearing

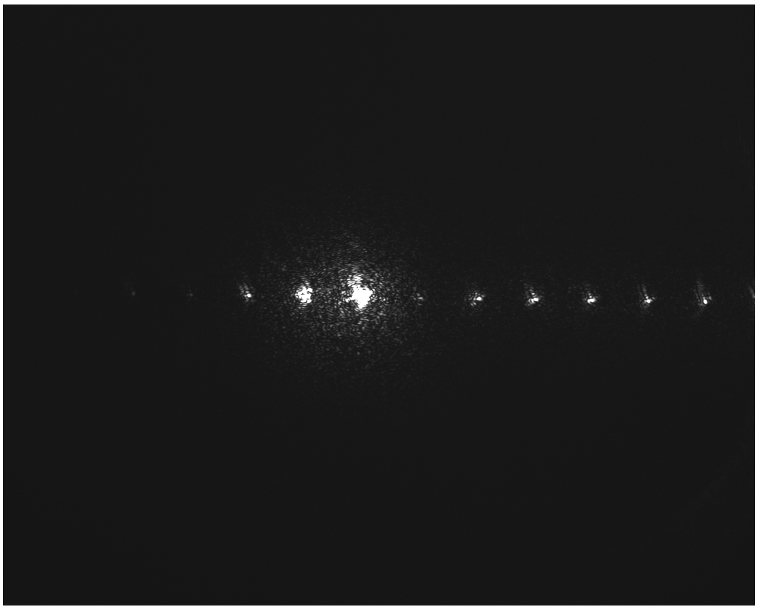

FIGURE 4.5: A diffraction grating was placed after L1, with L2 removed from the system, so that collimated light was incident on the grating. Light was redirected by the grating at various angles, and that light was collected by the MO. The irradiance maxima, called orders, occurred at angles which could be calculated from the diffraction grating equation, 4.1.

in the image recorded by the CMOS detector, shown in figure 4.5, therefore served as markers for pixels corresponding to particular scattering angles, according to equation4.1. Angles corresponding to pixels in between orders were determined by interpolation.

MATLAB software was created to fit the experimental scattergrams to a GLMT-based model. First, a set of theoretical scattergrams was generated based on GLMT. These scattergrams assumed a horizontally polarized excitation beam with a wavelength of 532nm incident on a sphere with a refractive index of 1.57826 (for polystyrene), surrounded by a medium with a refractive index of 1.00029 (air at STP). Scattergrams were generated for spheres with diameters ranging from 0.01µm to 8.00µm, in increments of 0.01µm. These scattergrams were divided into four sections called "bins," as shown in figure 4.6. The average scattered irradiance at each angle within a bin, for angles θ ranging from 8^o to 55^o, was plotted as a one-dimensional curve, as shown in figure 4.7. The same binning process was performed for each experimental scattergram. The plots of irradiance versus angle for each bin in the experimental scattergram were compared to the plot for the corresponding bin of each theoretical scattergram. Binning the scattergrams and comparing each of the four bins to theory, as opposed to representing the average scattered irradiance at each angle for the entire scattergram at once, allows for asymmetrical features of the scattergrams to be represented in the one-dimensional curves because each of the four curves can be different. The curves were compared to theory using a square error metric M^2 given by

$$M^2 = \sum_{\theta=8}^{\theta=55} \Big(I_{\text{exp}}(\theta) - I_{\text{theory}}(\theta) \Big)^2 + 10 \Big(I_{\text{exp}}(\theta) - I_{\text{theory}}(\theta) \Big)^2, \tag{4.2}$$

where $I_{\text{exp}}(\theta)$ is the irradiance value at a given angle for the experimental curve and $I_{\text{theory}}(\theta)$ is the irradiance value at that same angle for the theoretical curve. The theoretical diameter which resulted in the lowest value for M^2, summed across all four bins, was chosen as the best size estimate for the scatterer.

Scattergrams from 16 beads of each diameter and with each of the three various polarizations described above were fit to theory using the MATLAB software. The average size estimates for each bead size and for each polarization state are shown in Table 4.1, as well as the standard deviation between size estimates. The manufacturer-specified size distribution is also shown for each bead size. Comparing the scattergrams in figure 4.4 and the theoretical scattergrams in figure 2.1, which were generated assuming a horizontally-polarized incident beam, it is clear that the scattergrams recorded with the

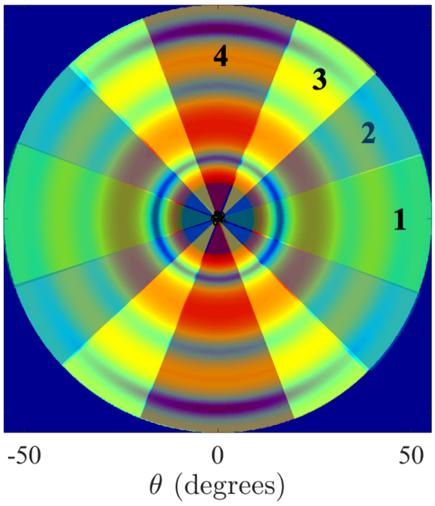

FIGURE 4.6: The scattergrams were divided into multiple sections called "bins." The average scattered irradiance at each angle θ within each bin was plotted as a one-dimensional curve which was fit to theory. The bins have been color coded in the above figure and numbered 1-4.

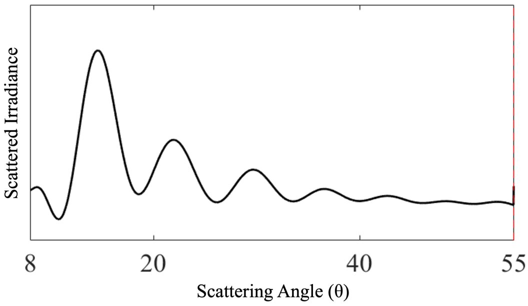

FIGURE 4.7: The average scattered irradiance at each angle within a bin was plotted as a one-dimensional curve. Shown is the theoretical curve for a polystyrene bead in air with a diameter of 5.18µm. The local irradiance maxima are clearly visible in the curve.

polarizer rotated by 90^o are oriented most similarly to the theoretical scattergrams used for comparison in the fitting code, which were generated assuming a horizontally-polarized incident beam. For each of the bead sizes, scattergrams recorded with the polarizer rotated by 90^o yielded a standard deviation which was more than 35% lower than that for scattergrams recorded with the polarizer in the other two orientations. In the case of the 5.00μm beads, the standard deviation was more than 60% smaller when the polarizer was at an angular displacement of 90^o as compared to when the polarizer was in the other two orientations. The standard deviation in each case was smaller than the manufacturer-specified range for the bead sizes.

Specified diameter:	1.755μm ± 0.022μm	
	Average diameter estimate	Standard deviation
LP rotated by 0^o	1.77μm	0.013μm
LP rotated by 45^o	1.75μm	0.022μm
LP rotated by 90^o	1.76μm	0.0082μm

Specified diameter:	5.027μm ± 0.047μm	
	Average diameter estimate	Standard deviation
LP rotated by 0^o	5.18μm	0.014μm
LP rotated by 45^o	5.18μm	0.014μm
LP rotated by 90^o	5.17μm	0.0054μm

TABLE 4.1: Average diameter estimates for the same two groups of 16 polystyrene beads, each group with a narrow, manufacturer-specified size distribution. Estimates were produced based on scattergrams with three different polarizations.

Fits for one representative bead of each size and for each of the polarization states of the excitation beam are shown in figure 4.7. Although the standard deviation between size estimates was the smallest for both bead sizes when the linear polarizer was rotated by 90^o, the theoretical curves resembled the experimental curves more closely in fits for the other polarizations. Therefore, because the standard deviation between fits for all polarizations was smaller than the manufacturer-specified range of sizes for the beads, the smaller standard deviation for one polarization is likely not indicative of more accurate size estimates. This will be discussed further in Section 4.5.

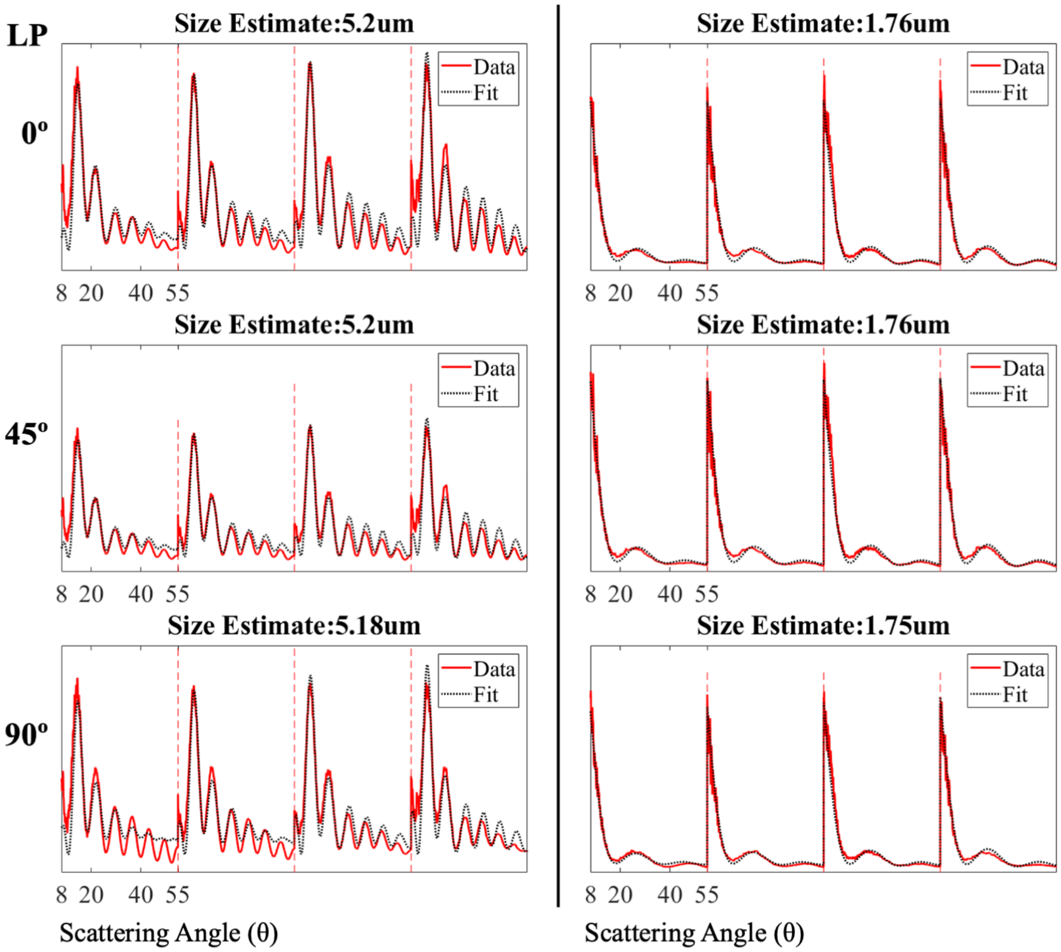

FIGURE 4.8: The average scattered intensity at each angle across each of the four bins was plotted as a one-dimensional curve and fit to theory. The dotted, black curve represents the best theoretical fit, and the solid, red curve represents data from the scattergram. Fits are shown for the same 5.00µm bead (left) and the same 1.75µm bead (right) for each of the three polarization states of the excitation beam. The four sections, delineated by a vertical, dashed, red line, correspond to the four bins of the scattergram. Each bin contains angles up to 55°.

4.5 Discussion and conclusion

The experiments described above demonstrate that the asymmetries exhibited in Mie scattering patterns are related to the polarization of the excitation light. The axes of symmetry of the scattergram rotate as the polarization rotates, and equation 3.37 was demonstrated empirically to be true. The results also support the hypothesis that the asymmetry predicted by Mie theory and GLMT is a feature distinctive to Mie scattering.

The axes of symmetry in the scattergrams from 5.00μm beads did not appear to be rotated by the expected 45^o when the linear polarizer was rotated by that amount. The degree of uncertainty with regard to the angular displacement of the polarizer, which was judged based on graduations etched into the rotation mount, was small (2^o), and it is unlikely that this uncertainty led to the discrepancy between the rotation of the polarizer and the observed rotation of the axes of symmetry in the scattered irradiance patterns.

It was also demonstrated that rotating the polarization of the excitation beam before recording scattergrams can affect the standard deviation in size estimates produced by fitting those scattergrams to theory. The standard deviation between size estimates for scattergrams recorded with the linear polarizer rotated by 90^o was smaller than that between size estimates for the other polarizations. However, it is unlikely that the reduced standard deviation is indicative of more accurate size estimates. First, the standard deviation between size estimates for all polarizations was less than the manufacturer-specified size range for the beads. Furthermore, as seen in figure 4.8, in the case of the 5.00μm beads, fit curves resembled the experimental curves more closely in fits for scattergrams recorded with the polarizer in its initial state than with the polarizer rotated by 90^o.

Chapter 5

Conclusions and potential applications of this work

The irradiance pattern of linearly polarized light scattered by a spherical scatterer with a diameter on the order of the wavelength of light is azimuthally asymmetrical but has two axes of reflective symmetry. It has been shown that the axes of symmetry are related to the polarization of the incident light and rotate as the polarization is rotated. This is reflected in mathematical models of the scattering by sine and cosine functions of the azimuthal angle ϕ, which are present in the two transverse components of the scattered electric field and have amplitudes which include different functions of the polar angle θ, as was explained in Chapter 3. This effect was demonstrated empirically by recording the scattering of light with differing polarization states by polystyrene beads, as was documented in Chapter 4.

A deeper understanding of elastic scattering of light by small particles has potential uses not just in the field of physics, but also in biology. As mentioned in Chapter 2, light scattering measurements can yield precise size estimates for subcellular structures like mitochondria. Changes in scattergrams can reflect size changes on the order of nanometers in organelles. This thesis explores a key aspect of such scattergrams, and a better understanding of the asymmetry may be advantageous to those who use angular scattering to produce size estimates for scatterers.

It was shown in Chapter 4 that rotating the polarization of the excitation beam before recording scattergrams can reduce the standard deviation between size estimates produced by fitting those scattergrams to theory. However, it is unlikely that this reduced standard deviation is indicative of more accurate size estimates, for reasons explained in Section 4.5.

5.1 Future research

Something that this thesis does not address is the physical mechanism which causes light to scatter asymmetrically off of a perfectly spherical scatterer. As stated in Chapter 3, the asymmetry is a direct mathematical consequence of Maxwell's equations. Therefore, it is likely that the mechanism is fundamental to electromagnetic theory in general. Furthermore, since the mechanism is not apparent on the scale of the wavelength of light, it is likely that the asymmetry results from interactions on the molecular or atomic level. The possibility that the asymmetry is exclusive to scatterers composed of polystyrene is undermined both by the presence of asymmetry in the simulated scattergrams of Chapter 4 and the fact that, while the only material-specific quality of either the scatterer or its surrounding medium explicitly considered by Mie theory is refractive index, it can be seen in Chapter 3 that an asymmetrical scattergram is still predicted unless the two sums (equations 3.2 and 3.3) in equation 3.1 are identical. It may also be worth investigating whether or not there exists a physically possible scenario in which the two sums would be identical.

It was noted in Chapter 4 that one of the asymmetrical features of the experimental scattergrams in figure 4.4 is two quadrants in which the irradiance falls to a lower value between local maxima than in the other two. It may be worth exploring whether fitting only these two quadrants to theory yields more accurate or consistent size estimates than fitting all four quadrants.

In the ongoing research led by Dr. Ashley Cannaday, which uses angular scattering theory to extract size estimates for the organelles within single cells, the polarization of the excitation beam will be rotated to precisely match the polarization assumed when generating theoretical scattergrams for the fitting code. It may also be advantageous for groups like Dr. Cannaday's to record scattering of light with two orthogonal polarizations for each specimen, and then to compare scattering for both polarizations to the appropriate theory in order to extract a size estimate. Averaging the size estimates for both polarizations may yield more accurate and consistent results because the effects of artifacts in the recorded images that do not change positions with rotation of the polarization of the incident beam may be suppressed. Furthermore, because of equation 3.37, the same set of theoretical scattergrams generated for the fitting code could be used when fitting both sets of recorded scattergrams. The theoretical scattergrams would simply have to be rotated by 90^o before comparison to one of the sets of experimental scattergrams.

Bibliography

[1] L. M. Pedrotti, *Introduction to Optics*, 3rd ed. Cambridge University Press, 2018.

[2] C. Jose Chirayil, J. Abraham, R. Kumar Mishra, S. C. George, and S. Thomas, "Chapter 1 - instrumental techniques for the characterization of nanoparticles", in *Thermal and Rheological Measurement Techniques for Nanomaterials Characterization*, ser. Micro and Nano Technologies, S. Thomas, R. Thomas, A. K. Zachariah, and R. K. Mishra, Eds., Elsevier, 2017, pp. 1–36, ISBN: 978-0-323-46139-9. DOI: `https://doi.org/10.1016/B978-0-323-46139-9.00001-3`. [Online]. Available: `https://www.sciencedirect.com/science/article/pii/B9780323461399000013`.

[3] U. of Iowa, *Rayleigh, Mie, and Optical Scattering*, 2006.

[4] W. J. Cottrell, J. D. Wilson, and T. H. Foster, "Microscope enabling multimodality imaging, angle-resolved scattering, and scattering spectroscopy", *Opt. Lett.*, vol. 32, no. 16, pp. 2348–2350, 2007. DOI: `10.1364/OL.32.002348`. [Online]. Available: `http://ol.osa.org/abstract.cfm?URI=ol-32-16-2348`.

[5] Z. J. Smith and A. J. Berger, "Validation of an integrated Raman- and angular-scattering microscopy system on heterogeneous bead mixtures and single human immune cells", *Appl. Opt.*, vol. 48, no. 10, pp. D109–D120, 2009. DOI: `10.1364/AO.48.00D109`. [Online]. Available: `http://ao.osa.org/abstract.cfm?URI=ao-48-10-D109`.

[6] A. E. Cannaday, J. E. Sorrells, and A. J. Berger, “Angularly resolved, finely sampled elastic scattering measurements of single cells: requirements for robust organelle size extractions”, *Journal of Biomedical Optics*, vol. 24, no. 08, p. 1, 2019, ISSN: 1083-3668. DOI: `10.1117/1.JBO.24.8.086502`. [Online]. Available: `https://www.spiedigitallibrary.org/journals/journal-of-biomedical-optics/volume-24/issue-08/086502/Angularly-resolved-finely-sampled-elastic-scattering-measurements-of-single-cells/10.1117/1.JBO.24.8.086502.full`.

[7] Z. J. Smith, “Integrated Raman and Angular Scattering of Single Biological Cells”, PhD thesis, University of Rochester, 2009.

[8] G. Mie, “Beiträge zur optik trüber medien, speziell kolloidaler metallösungen”, *Annalen der Physik*, vol. 330, no. 3, pp. 377–445, 1908.

[9] C. F. Bohren and D. R. Huffman, *Absorption and scattering of light by small particles*. Wiley, 1983, p. 530, ISBN: 9780471293408. [Online]. Available: `https://www.wiley.com/en-us/Absorption+and+Scattering+of+Light+by+Small+Particles-p-9780471293408`.

[10] G Gouesbet, G Grehan, and B Maheu, “Scattering of a gaussian beam by a mie scatter center using a bromwich formalism”, *Journal of Optics*, vol. 16, no. 2, pp. 83–93, 1985. DOI: `10.1088/0150-536x/16/2/004`. [Online]. Available: `https://doi.org/10.1088/0150-536x/16/2/004`.

[11] G. Grehan, B. Maheu, and G. Gouesbet, “Scattering of laser beams by mie scatter centers: Numerical results using a localized approximation”, *Appl. Opt.*, vol. 25, no. 19, pp. 3539–3548, 1986. DOI: `10.1364/AO.25.003539`. [Online]. Available: `http://ao.osa.org/abstract.cfm?URI=ao-25-19-3539`.

[12] G. Gouesbet, G. Gréhan, and B. Maheu, “Localized interpretation to compute all the coefficients gnm in the generalized lorenz–mie theory”, *J. Opt. Soc. Am. A*, vol. 7, no. 6, pp. 998–1007, 1990. DOI: `10.1364/JOSAA.`

7.000998. [Online]. Available: http://josaa.osa.org/abstract.cfm?URI=josaa-7-6-998.

[13] J. A. Lock and G. Gouesbet, "Rigorous justification of the localized approximation to the beam-shape coefficients in generalized lorenz-mie theory. I. on-axis beams", *J. Opt. Soc. Am. A*, vol. 11, no. 9, pp. 2503–2515, 1994. DOI: 10.1364/JOSAA.11.002503. [Online]. Available: http://josaa.osa.org/abstract.cfm?URI=josaa-11-9-2503.

[14] C. A. Lieber, S. K. Majumder, D. D. Billheimer, D. L. Ellis, and A. Mahadevan-Jansen, "Raman microspectroscopy for skin cancer detection in vitro", *Journal of biomedical optics*, vol. 13, no. 2, p. 024 013, 2009.

[15] T. C. B. Schut, P. J. Caspers, G. J. Puppels, A. Nijssen, F. Heule, M. H. Neumann, and D. P. Hayes, "Discriminating basal cell carcinoma from its surrounding tissue by raman spectroscopy", *Journal of investigative dermatology*, vol. 119, no. 1, pp. 64–69, 2002.

[16] M. Gniadecka, P. A. Philipsen, S. Wessel, R. Gniadecki, H. C. Wulf, S. Sigurdsson, O. F. Nielsen, D. H. Christensen, J. Hercogova, K. Rossen, *et al.*, "Melanoma diagnosis by raman spectroscopy and neural networks: Structure alterations in proteins and lipids in intact cancer tissue", *Journal of investigative dermatology*, vol. 122, no. 2, pp. 443–449, 2004.

[17] J. D. Wilson and T. H. Foster, "Mie theory interpretations of light scattering from intact cells", *Optics Letters*, vol. 30, no. 18, pp. 2442–2444, 2005.

[18] J. D. Wilson, C. E. Bigelow, D. J. Calkins, and T. H. Foster, "Light scattering from intact cells reports oxidative-stress-induced mitochondrial swelling", *Biophysical Journal*, vol. 88, no. 4, pp. 2929–2938, 2005, ISSN: 0006-3495. DOI: https://doi.org/10.1529/biophysj.104.054528.

[Online]. Available: https://www.sciencedirect.com/science/article/pii/S0006349505733452.

[19] J. D. Wilson, B. R. Giesselman, S. Mitra, and T. H. Foster, "Lysosome-damage-induced scattering changes coincide with release of cytochrome c", *Opt. Lett.*, vol. 32, no. 17, pp. 2517–2519, 2007. DOI: 10.1364/OL.32.002517. [Online]. Available: http://ol.osa.org/abstract.cfm?URI=ol-32-17-2517.

[20] Z. J. Smith and A. J. Berger, "Integrated Raman- and angular-scattering microscopy", *Opt. Lett.*, vol. 33, no. 7, pp. 714–716, 2008. DOI: 10.1364/OL.33.000714. [Online]. Available: http://ol.osa.org/abstract.cfm?URI=ol-33-7-714.

[21] Z. J. Smith, K. Chu, and S. Wachsmann-Hogiu, "Nanometer-Scale Sizing Accuracy of Particle Suspensions on an Unmodified Cell Phone Using Elastic Light Scattering", *PLoS ONE*, vol. 7, no. 10, C. M. Aegerter, Ed., e46030, 2012, ISSN: 1932-6203. DOI: 10.1371/journal.pone.0046030. [Online]. Available: https://dx.plos.org/10.1371/journal.pone.0046030.

[22] J. D. Wilson, W. J. Cottrell, and T. H. Foster, "Index-of-refraction-dependent subcellular light scattering observed with organelle-specific dyes", *Journal of Biomedical Optics*, vol. 12, no. 1, pp. 1 –10, 2007. DOI: 10.1117/1.2437765. [Online]. Available: https://doi.org/10.1117/1.2437765.

[23] A. Cannaday, S. Hanna, and J. Hoelle, "Construction of an inexpensive and portable angular scattering microscope for use in organelle size estimation", 2020.

[24] J. W. Goodman, *Introduction to Fourier Optics*, 4th ed. W.H. Freeman, 2017.